

1  
2  
3  
4 **1 Computational pipeline provides mechanistic understanding of Omicron variant**  
5 **2 of concern neutralizing engineered ACE2 receptor traps**  
6  
7  
8  
9

10 5 Soumya G. Remesh<sup>1,2</sup>, Gregory E. Merz<sup>2</sup>, Axel F. Brilot<sup>2</sup>, Un Seng Chio<sup>2</sup>, Alexandra N. Rizo<sup>2</sup>,  
11 6 Thomas H. Pospiech Jr.<sup>2</sup>, Irene Lui<sup>1</sup>, Mathew T. Laurie<sup>3</sup>, Jeff Glasgow<sup>1</sup>, Chau Q. Le <sup>1</sup>, Yun  
12 7 Zhang<sup>1</sup>, Devan Diwanji<sup>2</sup>, Evelyn Hernandez<sup>2</sup>, Jocelyne Lopez<sup>2</sup>, Komal Ishwar Pawar<sup>2</sup>, Sergei  
13 8 Pourmal<sup>2</sup>, Amber M. Smith<sup>2</sup>, Fengbo Zhou<sup>2</sup>, QCRG Structural Biology Consortium<sup>#</sup>, Joseph  
14 9 DeRisi<sup>3,4</sup>, Tanja Kortemme<sup>2,5,6,7</sup>, Oren S. Rosenberg<sup>2</sup>, Anum Glasgow<sup>8,\*</sup>, Kevin K. Leung<sup>1,\*</sup>, James  
15 10 A. Wells<sup>1,4,9,\*</sup> & Kliment A. Verba<sup>1,2,5,10,\*</sup>  
16  
17  
18

19 12 <sup>1</sup> Department of Pharmaceutical Chemistry, University of California, San Francisco, San  
20 13 Francisco, CA - 94158, USA

21 14 <sup>2</sup> QBI Coronavirus Research Group Structural Biology Consortium, University of California, San  
22 15 Francisco, CA - 94158,  
23 16 USA

24 17 <sup>3</sup> Department of Biochemistry and Biophysics, University of California San Francisco, San  
25 18 Francisco, CA - 94158, USA

26 19 <sup>4</sup> Chan Zuckerberg Biohub, San Francisco, CA - 94158,  
27 20 USA

28 21 <sup>5</sup> QBI, University of California, San Francisco, CA 94158, USA

29 22 <sup>6</sup> Department of Bioengineering and Therapeutic Sciences, University of California, San  
30 23 Francisco, CA - 94158, USA

31 24 <sup>7</sup> The University of California, Berkeley–University of California, San Francisco Graduate  
32 25 Program in Bioengineering, University of California, San Francisco, CA - 94158, USA

33 26 <sup>8</sup> Department of Biochemistry and Molecular Biophysics, Columbia University, New York, NY  
34 27 10032, USA

35 28 <sup>9</sup> Department of Cellular & Molecular Pharmacology, University of California San Francisco, San  
36 29 Francisco, CA - 94158, USA

37 30 <sup>10</sup> Lead contact

38 31 \* Correspondence: [kliment.verba@ucsf.edu](mailto:kliment.verba@ucsf.edu), [jim.wells@ucsf.edu](mailto:jim.wells@ucsf.edu), [kevin.leung@ucsf.edu](mailto:kevin.leung@ucsf.edu),  
39 32 [ag4522@cumc.columbia.edu](mailto:ag4522@cumc.columbia.edu)  
40  
41  
42  
43

44 33

45 34

46 35

47 36  
48  
49  
50  
51  
52  
53  
54  
55  
56  
57  
58  
59  
60  
61  
62  
63  
64  
65

1  
2  
3  
4 37

5  
6  
7 38 **Summary**

8  
9  
10 39 The SARS-CoV-2 Omicron variant, with 15 mutations in Spike receptor binding domain (Spike-  
11 RBD), renders virtually all clinical monoclonal antibodies against WT SARS-CoV-2 ineffective.  
12  
13 40 We recently engineered the SARS-CoV-2 host entry receptor, ACE2, to tightly bind WT-Spike-  
14  
15 41 RBD and prevent viral entry into host cells (“receptor traps”). Here we determine cryo-EM  
16  
17 42 structures of our receptor traps in complex with full length Spike. We develop a multi-model  
18  
19 43 pipeline combining Rosetta protein modeling software and cryo-EM to allow interface energy  
20  
21 44 calculations even at limited resolution and identify interface side chains that allow for high affinity  
22  
23 45 interactions between our ACE2 receptor traps and Spike-RBD. Our structural analysis provides a  
24  
25 46 mechanistic rationale for the high affinity (0.53 - 4.2nM) binding of our ACE2 receptor traps to  
26  
27 47 Omicron-RBD confirmed with biolayer interferometry measurements. Finally, we show that ACE2  
28  
29 48 receptor traps potently neutralize Omicron- and Delta- pseudotyped viruses, providing alternative  
30  
31 49 therapeutic routes to combat this evolving virus.  
32  
33 50

34  
35  
36  
37  
38  
39 51 **Keywords**

40  
41  
42  
43 52 SARS-CoV-2 Omicron variant, Spike, ACE2 receptor traps, protein therapeutics, pseudovirus  
44  
45 53 neutralization, cryo-EM, Rosetta  
46  
47  
48

49 54 **Introduction**

50  
51  
52  
53 55 The rapidly evolving SARS-CoV-2 virus has accumulated several mutations throughout the  
54  
55 56 pandemic. The Omicron (B.1.1.529) variant was first reported in November 2021 in South Africa  
56  
57 57 to have 37 mutations in its Spike glycoprotein and was quickly designated as a variant of concern  
58  
59 58 (VOC) by the World Health Organization (Viana et al., 2022; Walls et al., 2020). The Omicron  
60  
61  
62  
63  
64  
65

1  
2  
3  
4 59 Spike (S) glycoprotein receptor-binding domain (RBD) and N-terminal domain (NTD) harbor 15  
5  
6 60 and 11 mutations, respectively, leading to lower plasma neutralization in patients previously  
7  
8 61 infected with other SARS-CoV-2 variants or in fully vaccinated individuals (Cameroni et al., 2022;  
9  
10 62 Cao et al., 2022; Cele et al., 2021; Liu et al., 2022; Mannar et al., 2022; Planas et al., 2022;  
11  
12 63 VanBlargan et al., 2021; Wilhelm et al., 2021). Due to the antigenic shift in the Omicron variant,  
13  
14 64 currently only two out of eight clinical monoclonal antibody treatments, S309 (sotrovimab parent)  
15  
16 65 and the COV2-2196/COV2-2130 cocktail (cilgavimab/tixagevimab parents), retain appreciable  
17  
18 66 neutralizing capacity albeit reduced by 2-3 and 12-200 fold, respectively compared to  
19  
20 67 neutralization of Wuhan-hu-1 strain (Cameroni et al., 2022; Cao et al., 2022; Liu et al., 2022;  
21  
22 68 Mannar et al., 2022; Planas et al., 2022; VanBlargan et al., 2021). An earlier VOC, the B.1.617.2  
23  
24 69 Delta variant, also acquired 10 mutations in the Spike S glycoprotein, outcompeted other  
25  
26 70 circulating virus isolates, and enhanced transmission and pathogenicity while diminishing  
27  
28 71 antibody-based neutralization activity (McCallum et al., 2021; Mlcochova et al., 2021).  
29  
30 72 Interestingly, both the Delta- and Omicron RBD continue to bind the SARS-CoV-2 entry receptor,  
31  
32 73 human angiotensin converting enzyme 2 (ACE2), with almost 2-fold higher affinity than the wild-  
33  
34 74 type Spike-RBD (Cameroni et al., 2022; Mannar et al., 2022). Previously, we developed  
35  
36 75 engineered ACE2 “receptor traps” as viable candidates for SARS-CoV-2 virus neutralization  
37  
38 76 (Glasgow et al., 2020). The receptor traps were computationally designed and further affinity-  
39  
40 77 optimized by yeast display. The optimized ACE2 extracellular domains were fused to a human  
41  
42 78 IgG1 Fc domain to afford additional binding avidity and neonatal Fc receptor (FcRN) binding for  
43  
44 79 long circulating half-life. One advantage of using an ACE2 receptor trap as a therapeutic to treat  
45  
46 80 SARS-CoV-2 infections is that resistance evolved to ACE2 traps would also likely render the virus  
47  
48 81 unable to infect host cells via the ACE2 entry receptors. Thus, ACE2 traps could provide  
49  
50 82 alternative therapeutic strategies for the rapidly evolving SARS-CoV-2 virus.  
51  
52  
53  
54  
55  
56  
57  
58  
59 83 Our computationally designed (CVD293) and affinity matured (CVD313) ACE2 Fc-fusions have  
60  
61  
62  
63  
64  
65

1  
2  
3  
4 84 ~20-25-fold improved virus neutralization ability against WT-SARS-CoV-2 pseudotyped lentivirus  
5  
6 85 (Wuhan-hu-1 strain) compared to the WT-ACE2 Fc-fusion (Glasgow et al., 2020). However, the  
7  
8 86 structures of neither CVD293 nor CVD313 bound to WT-Spike-RBD have been captured, leaving  
9  
10 87 it an open question as to why the affinity matured ACE2 receptor traps bind WT-Spike-RBD  
11  
12 88 tighter. Here, we shortened the length of the linker between the ACE2 extracellular domain  
13  
14 89 (residues 18-740) of CVD313 and the Fc domain to ~13 amino acids to generate the construct  
15  
16 90 CVD432, which has an improved mammalian expression profile (total yield post purification of  
17  
18 91 CVD432 is ~2.5 times more than CVD313). We determined the cryo-EM structures of wild-type  
19  
20 92 full-length Spike protein (WT-fl-Spike) with either CVD293 or CVD432, which revealed molecular  
21  
22 93 details of the interactions between the ACE2 receptor traps and fl-Spike. Building on previous  
23  
24 94 approaches to provide ensemble models from cryo-EM maps (Herzik et al., 2019), we developed  
25  
26 95 a multi-model workflow to improve our confidence in the molecular interactions and the interaction  
27  
28 96 energies of the ACE2/RBD. This analysis allowed us to detect subtle interface differences  
29  
30 97 between the two receptor traps that were critical for the improved ACE2/RBD interface.  
31  
32 98 Furthermore, we used the cryo-EM structures together with Rosetta interface energy calculations  
33  
34 99 to model the interactions between our ACE2 receptor traps and Spike-RBD of Omicron VOC of  
35  
36 100 SARS-CoV-2, rapidly identifying the direct contact residues and predicting an even tighter  
37  
38 101 interaction than to the Spike-RBD of Wuhan-hu-1 strain. We validated these structural modeling  
39  
40 102 results by performing biolayer interferometry measurements. Finally, we showed that our ACE2  
41  
42 103 receptor traps potently neutralize Delta- and Omicron-SARS-CoV-2 pseudotyped viruses and  
43  
44 104 thus can serve as alternate therapeutic candidates against SARS-CoV-2 infections.  
45  
46  
47  
48  
49  
50  
51  
52

## 53 106 **Results**

54  
55 107

### 56 57 108 **Cryo-EM reconstructions of WT-fl-Spike trimer in complex with engineered ACE2 receptor** 58 59 60 109 **traps**

61  
62  
63  
64  
65

1  
2  
3  
4 110  
5  
6 111 To understand the molecular details of the interactions between the WT-fl-Spike and the  
7  
8  
9 112 engineered ACE2 receptor traps CVD293 and CVD432, we determined the cryo-EM structures  
10  
11 113 of these complexes (Figure 1). We confirmed that both CVD293 and CVD432 potently neutralize  
12  
13 114 WT-SARS-CoV-2 (Wuhan-hu-1 B.1 strain with D614G mutation only) pseudotyped virus (Figure  
14  
15 115 S1d). As noted previously for the WT-fl-Spike/WT-ACE2 complex (Yan et al., 2021; Zhou et al.,  
16  
17 116 2020a), we observed conformational heterogeneity for the complexes between WT-fl-Spike and  
18  
19  
20 117 the engineered ACE2 receptor traps, with the number of RBDs in the “up” or “down” conformation  
21  
22 118 per spike protein varying in the ACE2-bound state. The complex between WT-fl-Spike and  
23  
24 119 CVD293 showed a 1-RBD-up WT-fl-Spike with full ACE2 occupancy (~20%), an appreciable  
25  
26 120 percentage of 1-RBD-up WT-fl-Spike with partial ACE2 occupancy (~54%), a 2-RBD-up state with  
27  
28  
29 121 1-ACE2 occupancy (~15%) and a 1-RBD-up state with no ACE2 occupancy (Figure 1a) per trimer.  
30  
31 122 On the other hand, WT-fl-Spike and CVD432 showed a 1-RBD-up WT-fl-Spike with full ACE2  
32  
33 123 occupancy (~12%), a 2-RBD-up state with 2-ACE2 occupancy (~9%), all-RBD-down state, and  
34  
35 124 other partial- to no-ACE2 occupancy 1-RBD- and 2-RBD-up states (Figure 1b). While ACE2  
36  
37  
38 125 residues 18-614 were well resolved and could be fit into our cryo-EM maps of the complexes  
39  
40 126 between WT-fl-Spike/ACE2 receptor traps, we could not model the highly flexible collectrin  
41  
42 127 domain of the ACE2 traps (residues 615-740) as well as the Fc-domains. Nevertheless, the WT-  
43  
44 128 Spike-RBD/ACE2 receptor trap sub-region could be resolved at low to medium resolution.  
45  
46  
47 129  
48  
49 130 Local refinement of CVD293 or CVD432 (residues 18-614) with WT-Spike-RBD (residues 330-  
50  
51 131 541, Wuhan-hu-1 strain) generated maps of resolution ~3.8-4.8 Å and 3.4-3.8 Å, respectively, for  
52  
53 132 the interface residues (Figure 2a, S2, S3, S4 and S5). As described above, the high level of  
54  
55 133 heterogeneity between the 1-RBD-up and 2-RBD-up states for WT-fl-Spike with either CVD293  
56  
57  
58 134 or CVD432 made obtaining high resolution maps of the interface residues challenging. To better  
59  
60 135 understand the modalities of continuous protein motions within the 1-RBD-up or 2-RBD-up states,  
61  
62  
63  
64  
65

1  
2  
3  
4 136 we utilized 3D variability analyses (3DVA) (Punjani and Fleet, 2021) (Figure S1a-c). Both WT-fl-  
5  
6 137 Spike/CVD293 and WT-fl-Spike/CVD432 complexes showed considerable rotation relative to the  
7  
8 138 vertical axis (~5-7°) in the 1-RBD-up/ACE2 bound sub-region of the cryo-EM map (Figure S1a,  
9  
10 139 b). In contrast, the 2-RBD-up state of WT-fl-Spike/CVD432 showed lateral shift of the ACE2 bound  
11  
12 140 RBD sub-region of the cryo-EM map relative to the vertical axis of rotation (Figure S1c). This high  
13  
14 141 degree of variability in the ACE2 bound/RBD sub-region of the cryo-EM map further impeded high  
15  
16 142 resolution structure determination of the interface residues. Consequently, the precise rotamer  
17  
18 143 positions, especially of key interface residues for CVD293 (engineered mutations - K31F, H34I,  
19  
20 144 E35Q) or CVD432 (engineered mutations - K31F, N33D, H34S, E35Q) could not be obtained with  
21  
22 145 high confidence directly from the cryo-EM maps. (Figure 2b, c; cryo-EM consensus models are  
23  
24 146 shown fit to the cryo-EM maps).  
25  
26  
27  
28  
29

30  
31 **148 Improving confidence of the interface interactions in limited resolution cryo-EM maps**  
32  
33 **149 through Rosetta enabled multi-model workflow**  
34

35  
36 150  
37  
38 151 Inspired by a previous ensemble model refinement approach to improve confidence in maps with  
39  
40 152 resolution variation (Herzik et al., 2019), we developed a multi-model workflow which allowed for  
41  
42 153 calculation of an “average predicted interface energy” metric across an ensemble of models  
43  
44 154 consistent with the cryo-EM map in addition to the previously reported “average RMSD” metric.  
45  
46 155 Together, these metrics provided a statistics-based view of the ACE2/RBD interface (Figure 3a).  
47  
48 156 Briefly, 10-residue overlapping stretches of the ACE2 interface helix (residues 21 - 52) of each  
49  
50 157 cryo-EM consensus model (WT-Spike-RBD (330-541)/CVD293 (18-614) or WT-Spike-RBD (330-  
51  
52 158 541)/CVD432 (18-614)) were subjected to a CartesianSampler mover within Rosetta that samples  
53  
54 159 similar sequence and secondary structure fragments from within PDB and locally minimizes them  
55  
56 160 into the cryo-EM density, generating 2000 models for each 10-residue stretch. Each model was  
57  
58 161 then all-atom minimized within the cryo-EM map using FastRelax mover with a scoring term for  
59  
60  
61  
62  
63  
64  
65

1  
2  
3  
4 162 the model agreement with the cryo-EM map, as previously described (DiMaio et al., 2015). The  
5  
6 163 Rosetta parameters and scoring functions used were based on the estimated map resolution  
7  
8 164 (Wang et al., 2016). This refinement protocol was iteratively run to generate a total of ~8000  
9  
10 165 overlapping atomic models of the interface helix.  
11  
12  
13 166  
14  
15 167 We next ranked the atomic models based on total Rosetta scores ensuring good geometries (pick  
16  
17 168 top 200) and fits to the cryo-EM map (pick top 20 out of the above 200) for each 10-residue stretch  
18  
19 169 to select a total of 80 models for the entire interface helix. The average per residue side-chain  
20  
21 170 RMSDs and predicted average interface energy for all the residues of the interface helix for the  
22  
23 171 top selected cryo-EM based models were then calculated (Figure 3b,e). We compared average  
24  
25 172 per-residue side-chain RMSDs as we expected very small changes in the average backbone  
26  
27 173 RMSDs which can cause side-chain discrepancies being down-weighted in average full-  
28  
29 174 residue RMSDs. We superimposed the interface helix residues (residues 21-52) of the top 80  
30  
31 175 selected cryo-EM based models for both CVD293 and CVD432 to analyze the convergence of  
32  
33 176 the side-chain conformations and the intermolecular interaction with corresponding WT-Spike-  
34  
35 177 RBD residues. We observed that while the interface residues of CVD293 (F31, I34) or CVD432  
36  
37 178 (F31) with low average side-chain RMSD make well-defined hydrophobic interactions with  
38  
39 179 corresponding residues in WT-Spike-RBD (L455, F456, Y489), the high average side-chain  
40  
41 180 RMSD residue (Q35 of both CVD293 and CVD432) makes hydrogen bond interactions with  
42  
43 181 neighboring WT-Spike-RBD residue (Q493) in over 90% of the atomic models (Figure 3c, d). We  
44  
45 182 further noted that CVD432 high average side-chain RMSD residue, S34, can make both inter-  
46  
47 183 (with WT-Spike-RBD residue Y453) and intra-molecular hydrogen bonds (with backbone carbonyl  
48  
49 184 atoms of residues D30 or F31). We infer that the low average side-chain RMSD engineered  
50  
51 185 hydrophobic residues of the ACE2 receptor traps likely provide the key functional interactions  
52  
53 186 responsible for the improved binding affinity of the engineered receptor traps for WT-Spike-RBD.  
54  
55  
56  
57  
58  
59  
60  
61  
62  
63  
64  
65

1  
2  
3  
4  
5  
6  
7  
8  
9  
10  
11  
12  
13  
14  
15  
16  
17  
18  
19  
20  
21  
22  
23  
24  
25  
26  
27  
28  
29  
30  
31  
32  
33  
34  
35  
36  
37  
38  
39  
40  
41  
42  
43  
44  
45  
46  
47  
48  
49  
50  
51  
52  
53  
54  
55  
56  
57  
58  
59  
60  
61  
62  
63  
64  
65

187

188

189 **Analysis of the cryo-EM based models of CVD293 (18-614) and CVD432 (18-614) in complex**  
190 **with the WT-Spike-RBD (330-541)**

191

192 The comparison between the original computationally designed model of the CVD293/WT-Spike-  
193 RBD complex and the cryo-EM based models of the complex determined with our multi-model  
194 workflow revealed high overall structural agreement (Figure 2d). The average C $\alpha$ -RMSD between  
195 the computationally designed model and the experimentally solved cryo-EM consensus model of  
196 CVD293 (residues 18-614) was 0.93 Å, and the average C $\alpha$ -RMSD for the interface helix (ACE2  
197 residues 21-88, 322-329, 352-358 and Spike residues 444-446, 475-505) was 0.41 Å.

198

199 We next compared the calculated interface energy for the CVD293/WT-Spike-RBD interface in  
200 the design model and the cryo-EM based models. We found that the predicted interface energy  
201 is considerably lower for the CVD293 design model (-58 REU) than the average of 80 CVD293  
202 cryo-EM based models (-45 REU) (Figure 3e). This discrepancy between the predicted interface  
203 energy for the design model and the average interface energy calculated from the 80 cryo-EM  
204 based models is likely due to several differences in side-chain-mediated interactions involving  
205 designed residues. For example, isoleucine 34, a designed residue in CVD293, is predicted to  
206 contribute less to the interface energy in the cryo-EM based models (average from 80 atomic  
207 models of CVD293: -2.5 REU) than in the design model (-3 REU), despite strong agreement in  
208 the atomic coordinates for this residue across all cryo-EM based models (Figure 2d). The  
209 predicted interaction energy of I34 is worse in the cryo-EM models than the design model because  
210 its interaction partner across the interface, residue L455 of WT-Spike-RBD, universally adopts a  
211 different rotamer than the one in the original design model (Figure S7a).

212



1  
2  
3  
4 213 Residue Q35, another designed residue in CVD293, showed the largest observed average per-  
5  
6 214 residue side-chain RMSD among the designed positions on ACE2 in the cryo-EM based models  
7  
8 215 (Figure 3b). Although the Q35 side-chain often occupies a different rotamer in the cryo-EM based  
9  
10 216 models than in our original design model of CVD293, it still makes a hydrogen bond with the WT-  
11  
12 217 Spike-RBD residue Q493 as intended (Figure 3c). The WT-Spike-RBD residue Q493 shows  
13  
14 218 minimal conformational heterogeneity across the 80 cryo-EM based models of the complex  
15  
16 219 CVD293/WT-Spike-RBD, and it makes intramolecular hydrogen bonds with the carbonyl group of  
17  
18 220 the WT-Spike-RBD residue F490 to maintain the same loop conformation as seen in the complex  
19  
20 221 between WT-ACE2 and WT-Spike-RBD (Figure S7a). It is plausible that the minimal average  
21  
22 222 side-chain RMSD of residue Q493 and the overall similar loop conformation around residues  
23  
24 223 F490-Q493 in the complex CVD293/WT-Spike-RBD contribute to the observed conserved  
25  
26 224 hydrogen bond with residue Q35.  
27  
28  
29  
30  
31 225  
32  
33 226 Another WT-ACE2 residue, K31, was mutated to a phenylalanine in CVD293. Consequently, the  
34  
35 227 hydrogen bond between the WT-ACE2 residue K31 and the WT-Spike-RBD residue Q493 was  
36  
37 228 lost in the complex CVD293/WT-Spike-RBD. Instead of making this hydrogen bond, the designed  
38  
39 229 residue F31 in CVD293, with less than 1 Å average observed average side-chain RMSD, makes  
40  
41 230 good packing interactions with other aromatics at the WT-Spike-RBD/engineered ACE2 trap  
42  
43 231 interface as expected (Figure 3c). Overall, the average C $\alpha$ -RMSD between the computationally  
44  
45 232 designed model and the experimentally solved cryo-EM consensus model of CVD293 (residues  
46  
47 233 18-614) is close to 1 Å. However, using the cryo-EM based models of complex CVD293/WT-  
48  
49 234 Spike-RBD determined with our multi-model workflow, specific residue-pair interactions that were  
50  
51 235 critical to improving the WT-ACE2/WT-Spike-RBD interface with our computational design  
52  
53 236 strategy are revealed.  
54  
55  
56  
57  
58 237  
59  
60 238 We next wanted to understand why the affinity maturation of CVD293 in our yeast surface display  
61  
62  
63  
64  
65

1  
2  
3  
4  
5  
6  
7  
8  
9  
10  
11  
12  
13  
14  
15  
16  
17  
18  
19  
20  
21  
22  
23  
24  
25  
26  
27  
28  
29  
30  
31  
32  
33  
34  
35  
36  
37  
38  
39  
40  
41  
42  
43  
44  
45  
46  
47  
48  
49  
50  
51  
52  
53  
54  
55  
56  
57  
58  
59  
60  
61  
62  
63  
64  
65

239 campaign resulted in the I34S interface mutation in the construct CVD432, which has improved  
240 binding affinity for WT-Spike-RBD. We first generated a CVD432 “design” model by mutating the  
241 residue I34 in the CVD293 cryo-EM consensus model to a serine *in silico*. We also made an N33D  
242 mutation to CVD293 *in silico* even though this position is outside the RBD binding interface,  
243 because this mutation was also identified by yeast surface display in CVD432. The calculated  
244 interface energy for the CVD432 design model/WT-Spike-RBD interface is higher (-47 REU) than  
245 the average interface energy from 80 cryo-EM based models of the complex CVD432/WT-Spike-  
246 RBD (-53 REU) (Figure 3e). It can be inferred that simple *in silico* mutations do not provide a full  
247 explanation for the improved binding affinity between the engineered ACE2 trap and the WT-  
248 Spike-RBD, highlighting the value of the cryo-EM structure solution.

249 Comparing the cryo-EM based models of the complexes CVD293/WT-Spike-RBD and  
250 CVD432/WT-Spike-RBD, we find that the calculated interface energy from the average of 80 cryo-  
251 EM based models of the complex CVD432/WT-Spike-RBD is lower (-53 REU) than the average  
252 of 80 cryo-EM based models of the complex CVD293/WT-Spike-RBD (-45 REU) (Figure 3e). The  
253 decrease in calculated interface energy for the cryo-EM based models of the complex  
254 CVD432/WT-Spike-RBD as compared to that of the complex CVD293/WT-Spike-RBD is  
255 surprising for three reasons. First, S34 can adopt several different conformations (Figure 3d).  
256 Secondly, S34 makes weaker energetic contributions to the interface energy in all of the cryo-EM  
257 based models of the complex CVD432/WT-Spike-RBD than I34 in the complex CVD293/WT-  
258 Spike-RBD, regardless of the serine rotamer (Figure S6a). Third, S34 in CVD432 also has a  
259 higher average per-residue energy than I34 in CVD293 (Figure S6b). It is possible that a serine  
260 was enriched at position 34 in our directed evolution campaign using error-prone PCR because  
261 of the isoleucine parental codon, from which single base mutations could only lead to large  
262 hydrophobic amino acids, serine, threonine, or asparagine. Of these possibilities, serine is the  
263 smallest amino acid, and might have been favored simply to allow the other ACE2 residues to  
264 maintain favorable interactions with the RBD.

1  
2  
3  
4  
5  
6  
7  
8  
9  
10  
11  
12  
13  
14  
15  
16  
17  
18  
19  
20  
21  
22  
23  
24  
25  
26  
27  
28  
29  
30  
31  
32  
33  
34  
35  
36  
37  
38  
39  
40  
41  
42  
43  
44  
45  
46  
47  
48  
49  
50  
51  
52  
53  
54  
55  
56  
57  
58  
59  
60  
61  
62  
63  
64  
65

265

266

267

268

269

270

271

272

273

274

275

276

277

278

279

280

281

282

283

284

285

286

287

288

289

290

It appears that no individual residue at the interface is fully responsible for the improved interface energy in CVD432 cryo-EM based models over the CV293 design; rather, this improvement is the sum of several small improvements among many residues at the interface (Figure S6a). Interestingly, CVD432 contains an N33D mutation away from the interface which may be responsible for such overall stabilization of the interface. In all our models, N33D mutation breaks a hydrogen bond with the Q96 side-chain within ACE2 yielding a subtle shift of the neighboring residues towards the RBD (Figure S7b). This is correlated with subtly lower interface energies for these residues and lower total energy for D33 (Figure S6b, c). The N33D mutation was also observed to improve the RBD binding interaction in another ACE2 engineering study (Chan et al., 2020) and a computational analysis of ACE2 mutations (Chowdhury et al., 2020). Additionally, the interface helix may be stabilized by the main chain-side chain hydrogen bond between the S34 hydroxyl group and the F31 backbone carbonyl group in ACE2 (Figure 3d) that is not appropriately scored by Rosetta. Altogether, the improved SARS-CoV-2 neutralization by CVD432 compared to CVD293 is driven by mutations at the interface that improve binding in addition to stability-enhancing mutations outside the interface. As such, both protein stability and interface preorganization contribute to the overall stability of the receptor trap-RBD complex.

## **ACE2 receptor traps bind Omicron-RBD with increased affinity and neutralize the SARS-CoV-2 VOC**

Several of the 37 Omicron Spike mutations have been observed in other SARS-CoV-2 variants. For example, previous reports suggest that the N501Y mutation increases WT-ACE2 binding affinity while the K417N mutation decreases the WT-ACE2 binding affinity in some SARS-CoV-2 variants (Barton et al., 2021; Laffeber et al., 2021; Liu et al., 2021; Mannar et al., 2021; Tian et al., 2021; Zhu et al., 2021). Fourteen of the 37 mutations have not been reported previously in

1  
2  
3  
4 291 other variants but together were reported to improve the binding affinity ~2-3 fold between  
5  
6 292 Omicron-RBD and WT-ACE2 (Cameroni et al., 2022; Mannar et al., 2022; McCallum et al., 2022).  
7  
8 293 For example, while the Y505H mutation leads to loss in hydrogen bond interactions with WT-  
9  
10 294 ACE2 residue E37, there are several compensatory mutations in the Omicron-RBD. These  
11  
12 295 include Q493R and G496S, which result in new hydrogen bonds with WT-ACE2 residues E35  
13  
14 296 and K353, respectively and several others (Table S1, residue pairs colored green).  
15  
16  
17 297  
18  
19  
20 298 Our ACE2 receptor traps have >170-fold improved binding affinity for monomeric WT-Spike-RBD  
21  
22 299 compared to the binding affinity of WT-ACE2 for WT-Spike-RBD (Glasgow et al., 2020). To  
23  
24 300 evaluate if our ACE2 receptor traps would bind Omicron-RBD, we first generated models of  
25  
26 301 Omicron-RBD (330-530)/CVD293 (18-614) and Omicron-RBD (330-530)/CVD432 (18-614) by  
27  
28 302 superimposing and replacing WT-Spike-RBD in our respective cryo-EM local refinement of the  
29  
30 303 complexes with Omicron-RBD from the recently determined cryo-EM structure of Omicron-Spike  
31  
32 304 (330-530)/WT-ACE2 (19-613) (PDB ID: 7T9L, EMD-25761) (Figure 4a,b, panels on the right);  
33  
34 305 figure S8) and minimizing the complexes. Next, we calculated the Rosetta interface energies of  
35  
36 306 these models (Figure 4a,b; panels on the left). Although we predict an energy penalty for  
37  
38 307 engineered interface interaction residue pairs going from R493/E35 in Omicron-RBD/WT-ACE2  
39  
40 308 to R493/Q35 in Omicron-RBD/CVD293 or Omicron-RBD/CVD432 (in red in Figure 4a-b; panels  
41  
42 309 on the left), overall, we also predict improved binding affinities between the Omicron-RBD and  
43  
44 310 the engineered ACE2 receptor traps. Total interface energy for the interface residue pairs  
45  
46 311 contributing to the affinity between CVD293 or CVD432 to Omicron-RBD was calculated to be -  
47  
48 312 10.77 REU and -8.5 REU, respectively. For reference, the total interface energy for the interface  
49  
50 313 residue pairs contributing to the affinity between WT-ACE2 and Omicron-RBD was calculated to  
51  
52 314 be -4.99 REU. Potential contributions from interaction residue pairs L455/F31, Y489/F31 and  
53  
54 315 F31/R493 (in yellow in Figure 4a-b; panels on the left) and other residue pair interactions between  
55  
56 316 residue I34 of CVD293 or S34 of CVD432 and L455 of Omicron-RBD may be improving the  
57  
58  
59  
60  
61  
62  
63  
64  
65

1  
2  
3  
4 317 interface affinity (in blue in Figure 4a-b; panels on the left).

5  
6 318  
7  
8 319 To test whether improved predicted interface energies correspond to increased apparent binding  
9  
10 320 affinities, we assayed the binding affinity of CVD293 and CVD432 for Omicron-RBD by performing  
11  
12 321 biolayer interferometry (BLI). The BLI-determined dissociation constant ( $K_D$ ) between Omicron-  
13  
14 322 RBD/CVD293 ( $K_D = 4.2$  nM) or Omicron-RBD/CVD432 ( $K_D = 0.53$  nM) were measured to be 10-  
15  
16 323 and 100-fold lower than that for Omicron-RBD/WT-ACE2(18-740)-Fc-fusion, respectively (Figure  
17  
18 324 4c, Figure S9, Table S2). The hydrophobic interactions specific to Omicron-RBD/ACE2 receptor  
19  
20 325 trap complexes, along with the several compensatory mutations in Omicron-RBD/ACE2 interface  
21  
22 326 that are also maintained with the ACE2 receptor traps, likely result in the BLI-measured improved  
23  
24 327 affinity. Interestingly, CVD293 and CVD432 showed similar ( $K_D = 1.9$  nM) or about 100-fold ( $K_D =$   
25  
26 328  $0.071$  nM) lower  $K_D$  for Delta-RBD, respectively.

27  
28  
29 329  
30  
31 330 Finally, to determine whether the improved in vitro binding affinity also leads to higher potency in  
32  
33 331 viral neutralization, we tested the neutralization of Omicron (B.1.1.529) and Delta (B.1.617.2)  
34  
35 332 SARS-CoV-2 variants by our ACE2 receptor traps in pseudoviruses bearing these variants of  
36  
37 333 interest generated using recombinant vesicular stomatitis virus (VSV) expressing green  
38  
39 334 fluorescent protein (GFP) in place of the VSV glycoprotein (rVSV  $\Delta$ G-GFP). We compared the  
40  
41 335 neutralization of Delta and Omicron pseudoviruses to a control Spike-WT pseudovirus with a  
42  
43 336 D614G mutation. The pseudovirus neutralization assays demonstrated that both CVD293 and  
44  
45 337 CVD432 neutralize Delta (IC<sub>50</sub> = 1.4 nM, 1.6 nM, respectively) and Omicron (IC<sub>50</sub> = ND, 0.15nM,  
46  
47 338 respectively) pseudoviruses, with IC<sub>50</sub> values improved between 2-20-fold over Spike-WT (IC<sub>50</sub>  
48  
49 339 = 2.6 nM, 3.7 nM, respectively) pseudovirus (Figure 4d). Taken together, the results from the BLI  
50  
51 340 and pseudovirus neutralization assays suggest that our engineered ACE2 traps, although  
52  
53 341 computationally designed and affinity improved against WT-Spike-RBD, can still bind the rapidly  
54  
55 342 evolving SARS-CoV-2 variants with high affinity and potently block virus entry into cells.  
56  
57  
58  
59  
60  
61  
62  
63  
64  
65

1  
2  
3  
4  
5  
6  
7  
8  
9  
10  
11  
12  
13  
14  
15  
16  
17  
18  
19  
20  
21  
22  
23  
24  
25  
26  
27  
28  
29  
30  
31  
32  
33  
34  
35  
36  
37  
38  
39  
40  
41  
42  
43  
44  
45  
46  
47  
48  
49  
50  
51  
52  
53  
54  
55  
56  
57  
58  
59  
60  
61  
62  
63  
64  
65

## 343 Discussion

344

345 Over the course of the current pandemic, several neutralizing monoclonal antibodies (mAbs) have  
346 been identified and some have been evaluated clinically as therapeutic candidates against SARS-  
347 CoV-2 infection (Barnes et al., 2020a; Baum et al., 2020; Cohen et al., 2021; Dong et al., 2021;  
348 Gottlieb et al., 2021; Hansen et al., 2020; Jones et al., 2021; Shi et al., 2020; Zost et al., 2020).  
349 These mAbs are broadly categorized based on their ability to bind RBD in the “up” or “down”  
350 conformations on fl-Spike, engaging epitopes that can or cannot block ACE2 receptor binding to  
351 the RBD (Barnes et al., 2020b, 2020a; Liu et al., 2020; Shi et al., 2020; Tortorici et al., 2020).  
352 Several of the mAbs that bind the ACE2 recognition site (also called the receptor binding motif,  
353 RBM) within the RBD lost in-vitro neutralization activity against the Omicron-VOC (Cameroni et  
354 al., 2022; Mannar et al., 2022; Park et al., 2022). Interestingly, only the S2K146 mAb that binds  
355 SARS-CoV-2, SARS-CoV and other sarbecoviruses through ACE2 molecular mimicry retained  
356 neutralization activity against the Omicron-VOC (Cameroni et al., 2022; Park et al., 2022). This  
357 suggests that ACE2 specific binding epitope residues have a higher barrier for emergence of  
358 escape mutants.

359

360 We (Glasgow et al., 2020) and others (Chan et al., 2020; Higuchi et al., 2021; Lei et al., 2020)  
361 have explored “ACE2 decoy receptors” or “ACE2 receptor traps” that bind and block the RBD as  
362 an alternative approach for SARS-CoV-2 virus neutralization. Our ACE2 receptor traps were  
363 computationally designed, and affinity matured against the WT-Spike-RBD. In this study, we first  
364 determined the cryo-EM structures of the ACE2 receptor traps with the WT-fl-Spike to validate  
365 the mechanism of action for our computationally designed trap and to determine the molecular  
366 basis for the additional binding affinity improvement by the affinity-matured trap. Although the  
367 cryo-EM structures were informative, the limited resolution of ACE2/Spike-RBD interface residues  
368 prompted us to explore a multi-model cryo-EM structural workflow to circumvent the limited

1  
2  
3  
4  
5  
6  
7  
8  
9  
10  
11  
12  
13  
14  
15  
16  
17  
18  
19  
20  
21  
22  
23  
24  
25  
26  
27  
28  
29  
30  
31  
32  
33  
34  
35  
36  
37  
38  
39  
40  
41  
42  
43  
44  
45  
46  
47  
48  
49  
50  
51  
52  
53  
54  
55  
56  
57  
58  
59  
60  
61  
62  
63  
64  
65

369 resolution and leverage model ensembles for interface energy calculations.

370

371 From the cryo-EM structures and the derived multi-model workflow, we learned key lessons for  
372 designing strong binders: that distributed binding interactions across a protein-protein interface  
373 are more effective as compared to reliance on one or two important cross-interface interactions;  
374 and that it is important to prioritize the stability of all proteins individually in addition to the protein  
375 complex. Importantly, such stability may come from substitutions away from directly interacting  
376 residues, like N33D mutation in CVD432 that yields a lower energy conformation for that residue  
377 allowing for lower interface energies of surrounding residues. The data suggest that the stability  
378 and pre-organization of each protein at the interface is as important as the cross-interface  
379 interactions in the overall stability of the complex.

380

381 Recently, two engineered ACE2 decoy receptors have been reported to broadly neutralize SARS-  
382 CoV-2 variants including the Omicron-VOC (Ikemura et al., 2021; Zhang et al., 2022). These  
383 engineered decoy receptors neutralized the Omicron-VOC with IC50s comparable or even better  
384 than Omicron-VOC neutralizing mAbs such as VIR-7831. Apeiron's APN01, a wild-type ACE2  
385 soluble extracellular domain, has also shown promising results in early-phase clinical trials and  
386 retains the ability to neutralize multiple variants of concern (Wirnsberger et al., 2021).  
387 Furthermore, in a laboratory simulation of viral mutation under neutralizing selective pressure,  
388 another engineered ACE2 decoy receptor, 3n39v2 retained its neutralizing capacity over several  
389 passage cycles (Higuchi et al., 2021). Thus, soluble engineered ACE2 receptors have therapeutic  
390 value against SARS-CoV-2 variants and may continue to be relevant as this virus evolves further.

391

392 Application of the multi-model workflow increased our confidence in the atomic positions of  
393 computationally designed amino acids at the ACE2-Spike interface. This laid the groundwork for  
394 further improvements in the receptor trap design and allowed us to model interactions of the

1  
2  
3  
4 395 receptor traps with the Omicron-RBD. We experimentally verified the Omicron-RBD binding  
5  
6 396 interactions with the receptor traps using BLI and pseudovirus neutralization assays,  
7  
8  
9 397 demonstrating that our ACE2 receptor traps designed for neutralization of WT-fl-Spike from  
10  
11 398 SARS-CoV-2 remain robust to dozens of mutations in the VOCs. This is both surprising and  
12  
13 399 exciting since our computational design and affinity maturation optimized the binding interface of  
14  
15 400 ACE2 to selectively bind the targeted antigen, WT-Spike-RBD. These results are also in contrast  
16  
17  
18 401 to pan-specific antibodies that are affinity matured to be highly epitope- or antigen-specific binders  
19  
20 402 (Koerber et al., 2013; Mou et al., 2018; Zhou et al., 2020b). Perhaps, the particular hydrophobic  
21  
22 403 mutations at the binding interface of our ACE2 receptor traps make them more adaptable to Spike-  
23  
24 404 RBD mutations. Alternatively, as the virus evolves, its affinity for its entry receptor increases and  
25  
26  
27 405 fortuitously also to our ACE2 receptor traps.

28  
29 406  
30  
31 407 In addition to the RBM antigenic site, other mAbs with antigenic sites outside the RBM such as  
32  
33 408 Sotrovimab, S309, S2X259 and S2H97 also retained neutralization activity against Omicron-VOC  
34  
35 409 (Cameroni et al., 2022; Mannar et al., 2022; McCallum et al., 2022). A bifunctional antibody format  
36  
37  
38 410 called ReconAbs (receptor-blocking conserved non-neutralizing antibodies) was recently shown  
39  
40 411 to convert non-neutralizing antibodies to potent neutralizers of SARS-CoV-2 VOCs by linking the  
41  
42 412 “WT-ACE2 receptor” to a bispecific antibody targeting two non-overlapping conserved epitopes  
43  
44 413 (Weidenbacher et al., 2022). We envision future versions of our ACE2-receptor trap binders to be  
45  
46  
47 414 knob-in-hole bispecifics and other Fc-fusion formats with one engineered ACE2 arm and other  
48  
49 415 arm(s) as mAbs with antigenic sites outside the RBM, other non-neutralizing mAbs or Vh domains.

50  
51 416  
52  
53 417 Overall, this study exemplifies how technical advances in cryo-EM and computational protein  
54  
55 418 design methods can be combined towards improving the *design-build-test* cycle for engineering  
56  
57  
58 419 potent biotherapeutics, even for difficult targets such as the ACE2 complex with the SARS-CoV-  
59  
60 420 2 Spike protein. Furthermore, this workflow can be generalized for solving the cryo-EM structures

61  
62  
63  
64  
65



1  
2  
3  
4  
5  
6  
7  
8  
9  
10  
11  
12  
13  
14  
15  
16  
17  
18  
19  
20  
21  
22  
23  
24  
25  
26  
27  
28  
29  
30  
31  
32  
33  
34  
35  
36  
37  
38  
39  
40  
41  
42  
43  
44  
45  
46  
47  
48  
49  
50  
51  
52  
53  
54  
55  
56  
57  
58  
59  
60  
61  
62  
63  
64  
65

421 of other protein complexes and improving computational protein design protocols.

422

423 **Acknowledgements**

424

425 We thank members of the Wells Lab, particularly those working on COVID-19 projects, for their  
426 efforts and contributions. J.A.W. is supported by generous grants from NCI (R35 GM122451-01);  
427 the Chan-Zuckerberg Biohub, UCSF Program for Breakthrough Biomedical Research (PBBR);  
428 Fast Grants from Emergent Ventures at the Mercatus Center, George Mason University (#2154);  
429 and funding from The Harrington Discovery Institute (GA33116). A.G is supported by a grant from  
430 NIH (K99GM135529). K.A.V. is supported by Fast Grants from Emergent Ventures at the  
431 Mercatus Center, George Mason University and by QBI Independent Research Fellowship.

432 The structural biology portion of this work was performed by the QCRG (Quantitative Biosciences  
433 Institute Coronavirus Research Group) Structural Biology Consortium. Listed below are the  
434 contributing members of the consortium listed by teams in order of team relevance to the  
435 published work. Within each team the team leads are italicized (responsible for organization of  
436 each team, and for the experimental design utilized within each team), then the rest of team  
437 members are listed alphabetically.

438 **QCRG Structural Biology Consortium**

439 **CryoEM grid freezing/collection team:** *Axel F. Brilot, Gregory E. Merz, Alexandra N. Rizo,*  
440 *Caleigh M. Azumaya, Julian R. Braxton, Meghna Gupta, Fei Li, Kyle E. Lopez, Arthur Melo, Frank*  
441 *Moss, Joana Paulino, Thomas H. Pospiech Jr., Sergei Pourmal, Cristina Puchades, Amber M.*  
442 *Smith, Ming Sun, Paul V. Thomas, Feng Wang & Zanlin Yu*

443 **CryoEM data processing team:** *Axel F. Brilot, Gregory E. Merz, Alexandra N. Rizo, Soumya*  
444 *G. Remesh, Daniel Asarnow, Julian R. Braxton, Melody G. Campbell, Cynthia M. Chio, Un Seng*  
445 *Chio, Miles Sasha Dickinson, Devan Diwanji, Bryan Faust, Meghna Gupta, Nick Hoppe, Mingliang*

1  
2  
3  
4  
5  
6  
7  
8  
9  
10  
11  
12  
13  
14  
15  
16  
17  
18  
19  
20  
21  
22  
23  
24  
25  
26  
27  
28  
29  
30  
31  
32  
33  
34  
35  
36  
37  
38  
39  
40  
41  
42  
43  
44  
45  
46  
47  
48  
49  
50  
51  
52  
53  
54  
55  
56  
57  
58  
59  
60  
61  
62  
63  
64  
65

446 Jin, Fei Li, Junrui Li, Yanxin Liu, Henry C. Nguyen, Joana Paulino, Thomas H. Pospiech Jr., Sergei

447 Pourmal, Smriti Sangwan, Raphael Trenker, Donovan Trinidad, Eric Tse, Kaihua Zhang & Fengbo

448 Zhou

449 **Mammalian cell expression team:** *Evelyn Hernandez, Devan Diwanji, Amber M. Smith,*

450 *Caleigh M. Azumaya, Christian Billesboelle, Alisa Bowen, Melody G. Campbell, Nick Hoppe,*

451 *Yen-Li Li, Edmond Linossi, Jocelyne Lopez, Phuong Nguyen, Carlos Nowotny, Quynh Mai,*

452 *Hevatib Mehmood, Michael Paul, Cristina Puchades, Mali Safari, Smriti Sangwan, Kaitlin*

453 *Schaefer, Raphael Trenker, Tsz Kin Martin Tsui, Natalie Whitis & Jianhua Zhao*

454 **Protein purification team:** *Michelle Moritz, Sergei Pourmal, Daniel Asarnow, Caleigh M.*

455 *Azumaya, Cynthia M. Chio, Bryan Faust, Meghna Gupta, Raghav Kalia, Kate Kim, Tristan W.*

456 *Owens, Joana Paulino, Komal Pawar, Jessica K. Peters, Kaitlin Schaefer & Tsz Kin Martin Tsui*

457 **Crystallography team:** *Nadia Herrera, Huong T. Kratochvil, Ursula Schulze-Gahmen, Iris D.*

458 *Young, Justin Biel, Ishan Deshpande & Xi Liu*

459 **Bacterial expression team:** *Amy Diallo, Meghna Gupta, Jen Chen, Loan Doan, Sebastian*

460 *Flores, Mingliang Jin, Huong T. Kratochvil, Victor L. Lam, Yang Li, Megan Lo, Gregory E. Merz,*

461 *Joana Paulino, Aye C. Thwin, Erron W. Titus, Zanlin Yu, Fengbo Zhou & Yang Zhang*

462 **Infrastructure team:** *David Bulkley, Arceli Joves, Almarie Joves, Liam McKay, Mariano Tabios*

463 *& Eric Tse*

464 **Leadership team:** *David A. Agard, Yifan Cheng, James S. Fraser, Adam Frost, Natalia Jura,*

465 *Tanja Kortemme, Nevan J. Krogan, Aashish Manglik, Oren S. Rosenberg, Daniel R.*

466 *Southworth, Robert M. Stroud & Kliment A. Verba*

467

468 **Author Contributions**

469

470 Conceptualization, K.A.V, A.G., S.G.R, T.K., K.K.L., J.A.W.; methodology (cryo-EM data

1  
2  
3  
4 471 collection), G.E.M, A.F.B., A.N.R., T.H.P.; methodology (cryo-EM structure solution), G.E.M,  
5  
6 472 A.F.B., U.S.C., S.G.R.; methodology (cryo-EM based multi-model workflow), S.G.R. and K.A.V.;  
7  
8 473 methodology (Rosetta energy calculations), A.G.; methodology (cloning, protein expression and  
9  
10 474 purification), J.G., S.G.R., I.L., C.Q.L., Y.Z., E.H., D.D., S.P., A.M.S., J.L., K.I.P.; methodology  
11  
12 475 (Bilayer interferometry), I.L.; methodology (pseudovirus generation), M.T.L., J.D.; methodology  
13  
14 476 (pseudoviral assay), S.G.R.; writing—original draft, S.G.R., A.G. K.A.V., T.K., J.A.W., K.K.L.;  
15  
16 477 visualization, S.G.R., A.G., K.A.V.; supervision; K.A.V., A.G., K.K.L., J.A.W.; funding acquisition,  
17  
18 478 K.A.V., A.G., J.A.W  
19  
20  
21

22 479

23  
24 480 **Declaration of Interest**

25  
26 481

27  
28 482 None declared

29  
30 483

31  
32 484

33  
34 485

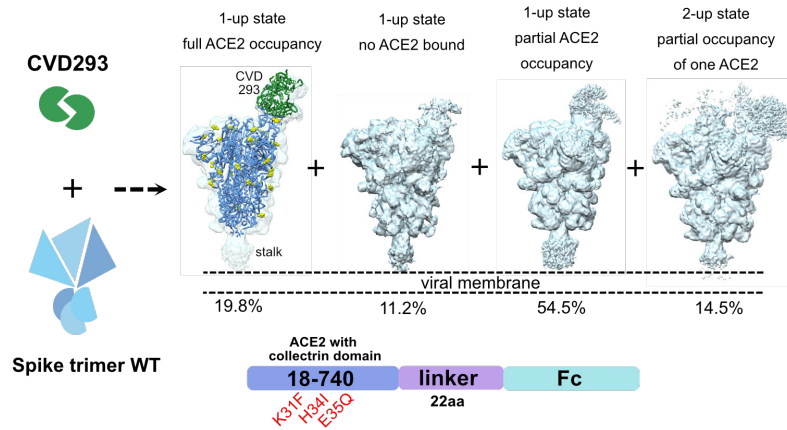
35  
36 486

37  
38  
39  
40  
41  
42  
43  
44  
45  
46  
47  
48  
49  
50  
51  
52  
53  
54  
55  
56  
57  
58  
59  
60  
61  
62  
63  
64  
65

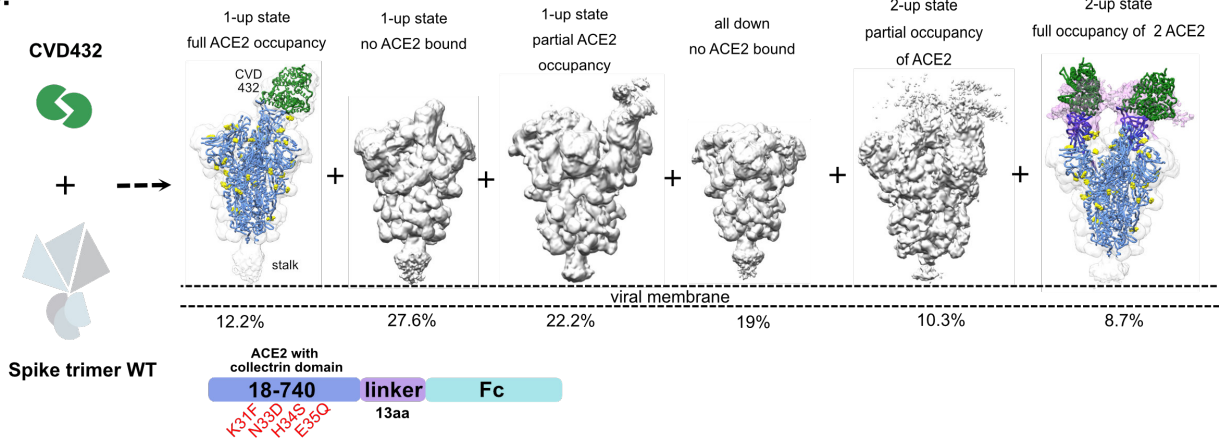
1  
2  
3  
4  
5  
6  
7  
8  
9  
10  
11  
12  
13  
14  
15  
16  
17  
18  
19  
20  
21  
22  
23  
24  
25  
26  
27  
28  
29  
30  
31  
32  
33  
34  
35  
36  
37  
38  
39  
40  
41  
42  
43  
44  
45  
46  
47  
48  
49  
50  
51  
52  
53  
54  
55  
56  
57  
58  
59  
60  
61  
62  
63  
64  
65

487 Figure 1.

a.



b.



488

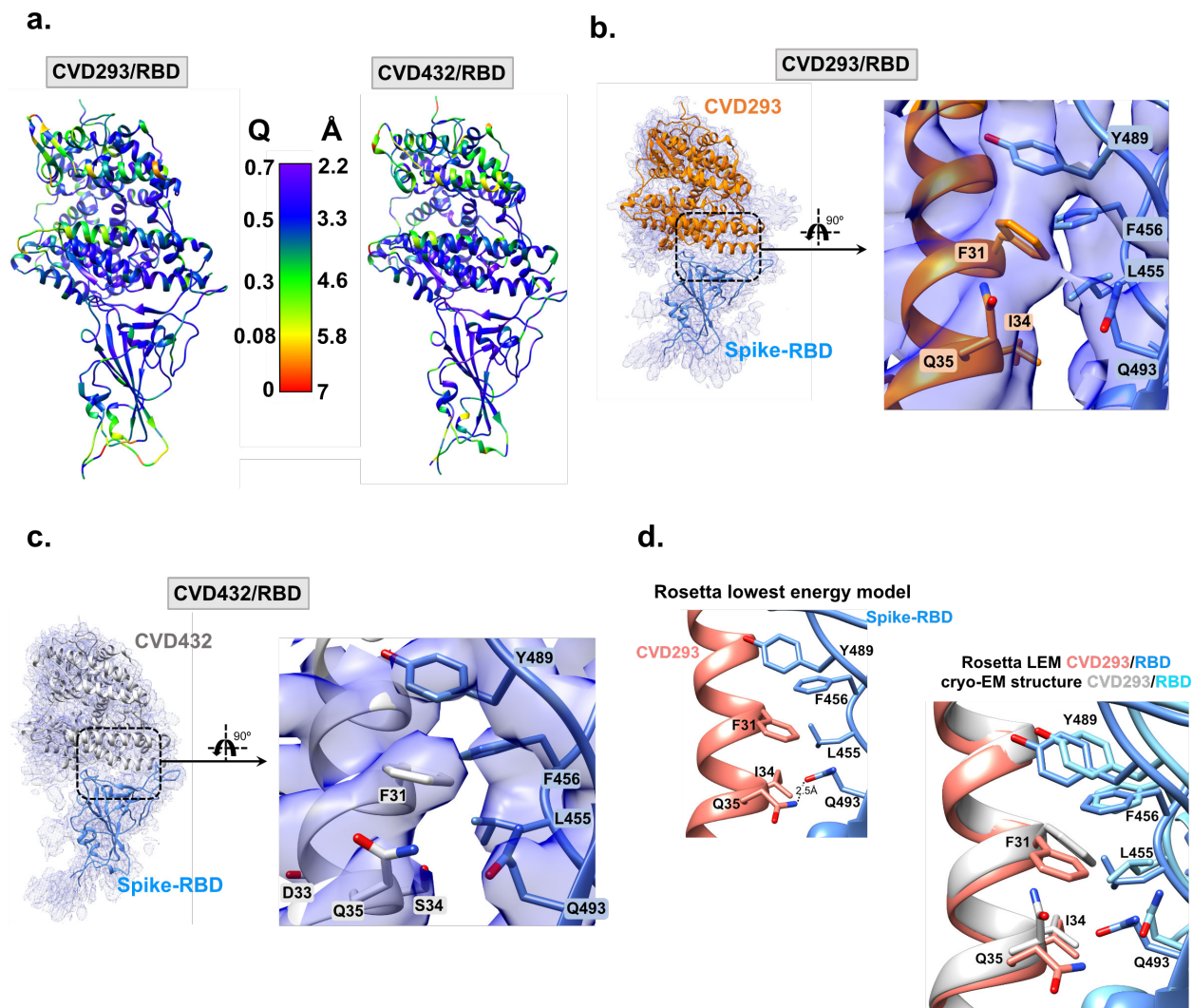
489 **Figure 1. Cryo-EM reconstruction of WT-fl-Spike with computationally designed, CVD293**  
490 **or linker variant of the affinity matured variant, CVD432**

491 **a-b.** Cryo-EM reconstructions of WT-fl-Spike with CVD293 or CVD432 showing the heterogeneity  
492 in distribution of all RBD down, 1-RBD- or 2-RBD-up states and variable ACE2 occupancy. Also  
493 shown is schematic of the primary structure of CVD293 or CVD432 and the engineered mutations,  
494 colored by domain.

495

496

497 Figure 2.



498  
499 **Figure 2. Cryo-EM reconstruction of WT-Spike-RBD with engineered ACE2 Fc-fusions**  
500 **reveal contributions from hydrophobic interactions at RBD-ACE2 interface**

501 **a.** WT-Spike-RBD/CVD293 and WT-Spike-RBD/CVD432 models colored by estimated per  
502 residue Q-score ranging from 0 (red) to 0.7 (purple). The color bar shows corresponding  
503 estimated resolution in Å for each Q-score. Expected Q-score for 3.5 Å map is 0.49 and expected  
504 Q-score for 3.36 Å map is 0.52. **b-c.** Cryo-EM reconstructions of WT-Spike-RBD with either  
505 CVD293 or CVD432 show favorable  $\pi$ - $\pi$  stacking interactions between WT-Spike-RBD residue  
506 Y489 and engineered ACE2 residue F31. Additionally, there are also hydrophobic interactions

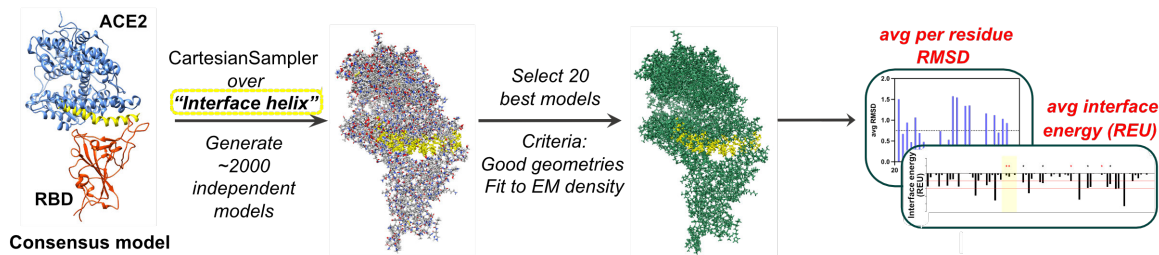
1  
2  
3  
4  
5  
6  
7  
8  
9  
10  
11  
12  
13  
14  
15  
16  
17  
18  
19  
20  
21  
22  
23  
24  
25  
26  
27  
28  
29  
30  
31  
32  
33  
34  
35  
36  
37  
38  
39  
40  
41  
42  
43  
44  
45  
46  
47  
48  
49  
50  
51  
52  
53  
54  
55  
56  
57  
58  
59  
60  
61  
62  
63  
64  
65

507 between WT-Spike-RBD residue L455 and CVD293 residue I34 are also seen. Hydrogen bond  
508 interactions between WT-Spike-RBD residue Q493 and CVD293 or CVD432 residue Q35 are not  
509 apparent in the cryo-EM consensus model. **d.** The Rosetta lowest energy model for CVD293 is  
510 overlaid with the cryo-EM model. Both models show hydrophobic and hydrogen bond interactions  
511 between CVD293 and WT-Spike-RBD residues that contribute to improved interface energy  
512 (REU) compared to the ACE2-WT Spike RBD interaction.

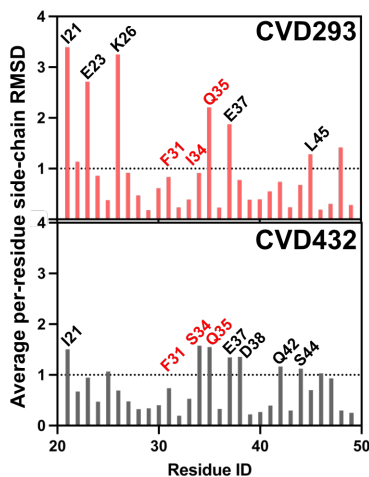
513  
514

515 Figure 3.

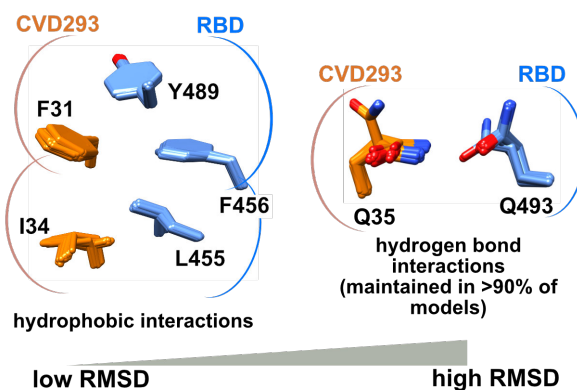
a.



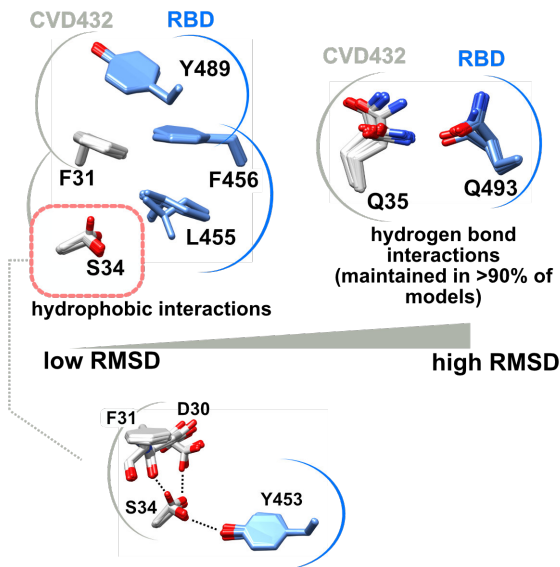
b. Average per-residue side-chain RMSD for Interface helix



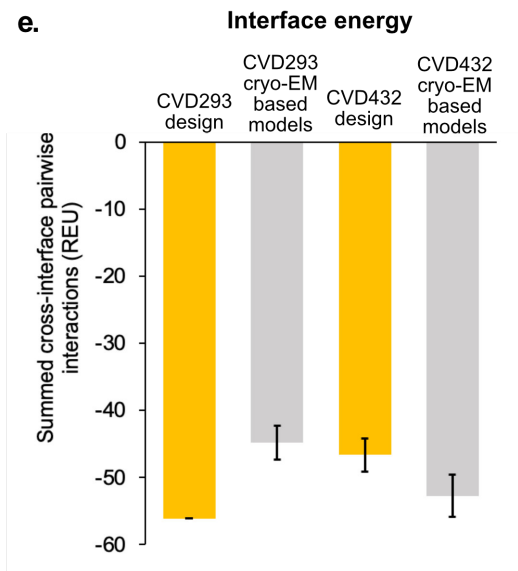
c.



d.



e.



516

1  
2  
3  
4  
5  
6  
7  
8  
9  
10  
11  
12  
13  
14  
15  
16  
17  
18  
19  
20  
21  
22  
23  
24  
25  
26  
27  
28  
29  
30  
31  
32  
33  
34  
35  
36  
37  
38  
39  
40  
41  
42  
43  
44  
45  
46  
47  
48  
49  
50  
51  
52  
53  
54  
55  
56  
57  
58  
59  
60  
61  
62  
63  
64  
65

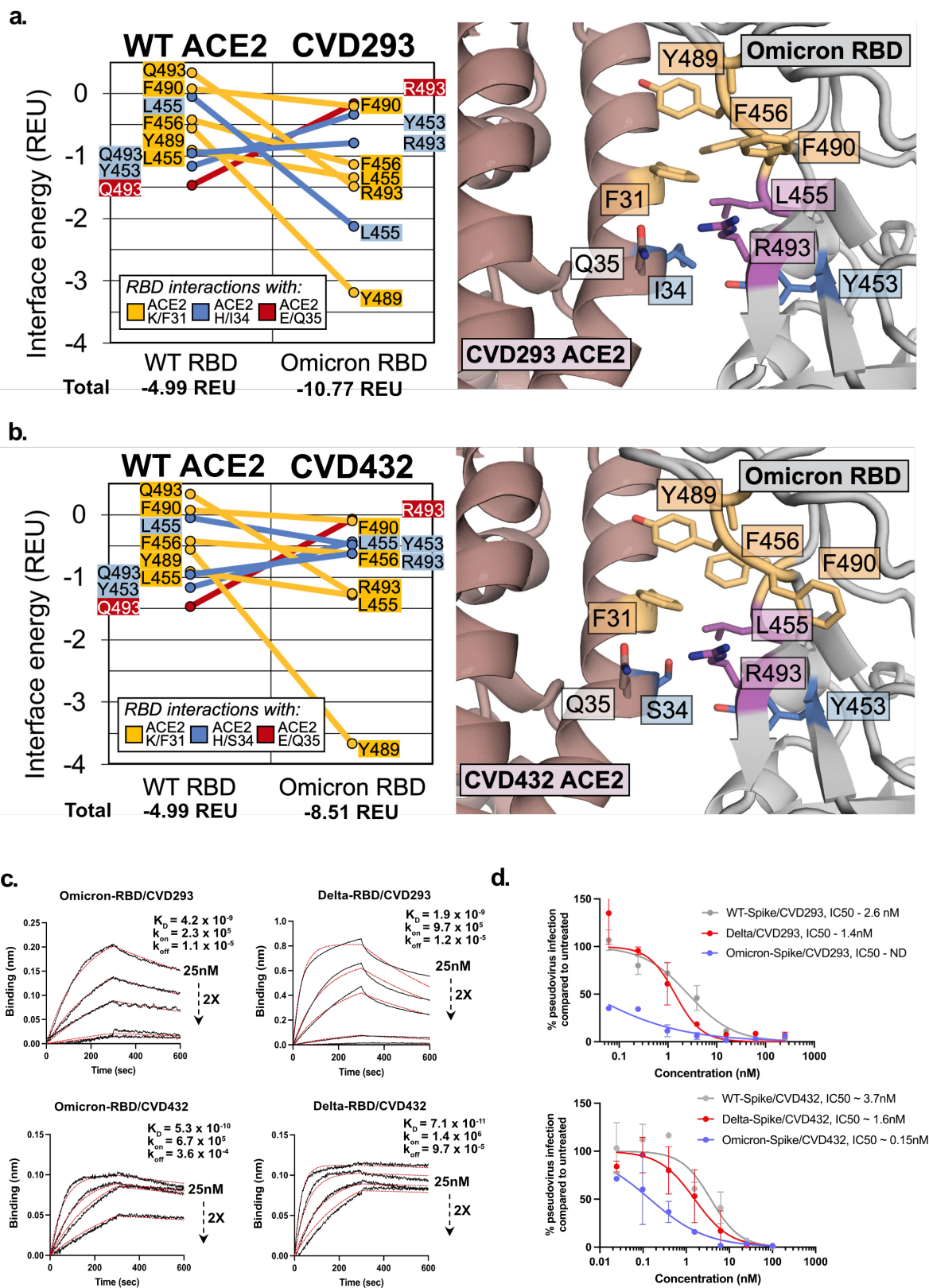
**517 Figure 3. Multi-model pipeline improves confidence of molecular interactions at the**  
**518 interface residues in cryo-EM derived models of WT-Spike-RBD with engineered ACE2 Fc-**  
**519 fusions**

**520 a.** Multi-model pipeline with average Rosetta interface energy and average per-residue side-chain  
**521** RMSD metrics for interface residue rotamer positions. **b.** Average per-residue side chain RMSD  
**522** for interface helix residues of CVD293 and CVD432 **c-d.** Superposition of critical interface  
**523** residues of the top 80 selected cryo-EM based models for CVD293 and CVD432. **e.** Average  
**524** Rosetta interface energy for CVD293 design model, CVD293 cryo-EM based models, CVD432  
**525** design model and CVD432 cryo-EM based models.

**526**  
**527**



528 Figure 4.



529

1  
2  
3  
4 **530 Figure 4. Binding to Omicron- and Delta-RBD and neutralization of Omicron- and Delta-**  
5  
6 **531 SARS-CoV-2 VOCs by CVD293 and CVD432**

7  
8 **532 a-b.** Left panel - Predictions based on Rosetta interface energy calculations suggest that  
9  
10 **533** Omicron-RBD binds CVD293 and CVD432 with high affinity. Residue pair interactions of RBD  
11  
12 **534** residues with CVD293/CVD432 residue F31 (yellow), with residue I34/S34 (blue) and with residue  
13  
14 **535** Q35 (red) are shown. Right panel - Zoomed in view of the interface of the models Omicron-  
15  
16 **536** RBD/CVD293 and Omicron-RBD/CVD432. Wheat-colored residues indicate RBD interactions  
17  
18 **537** ACE2 K/F31. Blue residues indicate RBD interactions with ACE2 H/I/S34. Magenta residues  
19  
20 **538** indicate RBD interactions with more than one engineered ACE2 residue **c.** Biolayer interferometry  
21  
22 **539** measurements for CVD293 or CVD432 interactions with Omicron- or Delta-RBD. **d.** CVD293 and  
23  
24 **540** CVD432 potently neutralize vesicular stomatitis virus (VSV) pseudotyped with SARS-CoV2  
25  
26 **541** Omicron- and Delta-Spike. Error bars represent standard deviation over all technical replicates  
27  
28  
29  
30  
31 **542** from two biological replicates.

32  
33 **543**

34  
35 **544**  
36  
37  
38  
39  
40  
41  
42  
43  
44  
45  
46  
47  
48  
49  
50  
51  
52  
53  
54  
55  
56  
57  
58  
59  
60  
61  
62  
63  
64  
65

1  
2  
3  
4  
5  
6  
7  
8  
9  
10  
11  
12  
13  
14  
15  
16  
17  
18  
19  
20  
21  
22  
23  
24  
25  
26  
27  
28  
29  
30  
31  
32  
33  
34  
35  
36  
37  
38  
39  
40  
41  
42  
43  
44  
45  
46  
47  
48  
49  
50  
51  
52  
53  
54  
55  
56  
57  
58  
59  
60  
61  
62  
63  
64  
65

## 545 **Materials and Methods**

546

### 547 **Cloning, Expression and Purification of Protein Constructs**

548 WT-fl-Spike plasmid was a generous gift from the Pak lab (Chan Zuckerberg Initiative Biohub)  
549 and Krammer lab (Icahn School of Medicine at Mount Sinai). WT-fl-Spike construct has an N-  
550 terminal spike protein signal peptide, a trimerization domain and C-terminal 6XHis-tag. WT, Delta-  
551 , Omicron-SARS-CoV-2 spike RBD and ACE2 variants (CVD293) were cloned into a pFUSE-  
552 based vector with Zeocin antibiotic resistance marker for mammalian expression using the Gibson  
553 method. The SARS-CoV-2 spike RBD construct has an IL2 secretion signal followed by the gene  
554 of interest, a Gly-Ser linker, a TEV protease cut site, a Gly-Ser linker, an 8X His-tag and an  
555 Avitag. CVD293 was cloned into a similar construct with N-terminal IL2 secretion signal followed  
556 by ACE2 with the relevant mutations (K31F, H34I, E35Q), a Gly-Ser linker, a TEV protease cut  
557 site, a Gly-Ser linker, a human IgG1 hinge and Fc, and AviTag. Construct CVD432 was purchased  
558 from Twist Bioscience ([www.twistbioscience.com](http://www.twistbioscience.com)). The construct has an Ampicillin resistance  
559 marker, an N-terminal ACE2 secretion signal followed by ACE2 with the relevant CVD313  
560 mutations (K31F, N33D, H34S, E35Q), a short Gly-Ser linker, a human IgG1 hinge and Fc. Also,  
561 the H345L mutation in CVD313 was reverted to wildtype residue, histidine.

562

563 WT-fl-Spike protein was purified based on the previously described protocol (Weinberg et al.,  
564 2021) 30ml of ExpiCHO-S cells at 6M cells/mL were transfected with 1ug/mL of the spike WT  
565 using the ExpiCHO™ Expression System Kit (Gibco, catalog # A29133) following the  
566 manufacturer's Standard protocol. Briefly, the transfected cells were shaken at 37°C and 8% CO<sub>2</sub>  
567 and 18 hours post-transfection, the cultures were supplemented with ExpiCHO™ Feed and  
568 ExpiFectamine™ CHO Enhancer and continued to be shaken at 37°C and 8% CO<sub>2</sub> for up to 10  
569 days. The supernatant with secreted spike protein was collected by centrifugation of the culture  
570 at 4000xG for 15 mins. The media was filtered using a 0.42µM filter and was transferred to a 50

1  
2  
3  
4  
5  
6  
7  
8  
9  
10  
11  
12  
13  
14  
15  
16  
17  
18  
19  
20  
21  
22  
23  
24  
25  
26  
27  
28  
29  
30  
31  
32  
33  
34  
35  
36  
37  
38  
39  
40  
41  
42  
43  
44  
45  
46  
47  
48  
49  
50  
51  
52  
53  
54  
55  
56  
57  
58  
59  
60  
61  
62  
63  
64  
65

571 mL centrifuge tube. The sample was then mixed with 2 mL washed Ni-Excel resin (Millipore  
572 Sigma, catalog # GE17371201) pre-equilibrated with 10 mM Tris/HCl, pH 8.0, 200 mM NaCl and  
573 placed on a rocker for 1 hour at room temperature. After binding, the sample was washed with 25  
574 bed volumes of Wash buffer (10 mM Tris/HCl, pH 8.0, 200 mM NaCl, 10 mM imidazole), and  
575 eluted with 7 bed volumes of elution buffer (10 mM Tris pH 8.0, 200 mM NaCl, 500 mM imidazole)  
576 into separate 2 mL centrifuge tubes. The eluent was concentrated, filtered, and a final SEC  
577 polishing step was performed on Superose<sup>®</sup> 6 10/300 Increase (Millipore Sigma, catalog # GE17-  
578 5172-01) pre-equilibrated in 10 mM HEPES pH 8.0, 200 mM NaCl at 4°C.

579  
580 WT, Delta-, Omicron-SARS-CoV-2 spike RBD and ACE2 variants (CVD293 and CVD432) were  
581 expressed in high density Expi293F<sup>TM</sup> cells in Expi293<sup>TM</sup> expression media following  
582 manufacturer's protocol (Expi293 Expression System, ThermoFisher Scientific). Briefly, 3x10<sup>6</sup>  
583 cell/ml at >95% viability in 25ml media were transfected with ~30ug of DNA using  
584 ExpiFectamine<sup>TM</sup> transfection reagent and Opti-MEM<sup>TM</sup> I medium. The transfected cells were  
585 incubated at 37 °C, 8% CO<sub>2</sub> on an orbital shaker, supplemented with ExpiFectamine<sup>TM</sup> 293  
586 Transfection Enhancer 1 and ExpiFectamine<sup>TM</sup> 293 Transfection Enhancer 2 about 18-22 hours  
587 post-transfection and continued to be incubated at 37 °C, 8% CO<sub>2</sub> on an orbital shaker for  
588 additional 4-5 days. Cells were harvested 4-5 days post-transfection, centrifuged at 3000 x g for  
589 15 minutes, supernatant collected and filtered through 0.22µM syringe filter. Proteins were  
590 neutralized with 10X phosphate buffered saline (PBS, 0.01 M phosphate buffer, 0.0027 M KCl  
591 and 0.137 M NaCl, Millipore Sigma P4417-100TAB), pH 7.4 to a final concentration of 2.5x PBS  
592 (342.5 mM NaCl, 6.75 mM KCl and 29.75 mM phosphates). SARS-CoV-2 RBDs were purified  
593 using cobalt-based immobilized metal affinity chromatography followed by buffer exchange into  
594 1X PBS using a Superdex 200 Increase 10/300 GL column (Cytiva). Fc-fused ACE2 proteins  
595 were purified on HiTrap Protein A column (GE Healthcare) and eluted with 50 mM Tris pH 7.2, 4  
596 M MgCl<sub>2</sub> and buffer exchanged into 1X PBS. The protein concentrations were estimated based

1  
2  
3  
4 597 on the protein absorbance at 280 nm with a spectrophotometer (Nanodrop One, Thermo).  
5

6 598 All the proteins were >95% pure as determined by SDS-Page gel electrophoresis. The proteins  
7  
8 599 were aliquoted, flash frozen, and stored in -80°C.  
9

10  
11 600  
12  
13 601 **Cryo-electron Microscopy Sample Preparation and Data Collection** - Purified WT-fl-Spike at  
14

15 602 2  $\mu\text{M}$  was mixed with either CVD293 (at 2.5  $\mu\text{M}$ ) or CVD432 (at 3  $\mu\text{M}$ ) just prior to plunge freezing.  
16

17 603 300 mesh 1.2/1.3R UltraAufoil grids were glow discharged at 15 mA for 30 seconds. Vitrification  
18

19  
20 604 was done using FEI Vitrobot Mark IV (ThermoFisher) set up at 4°C and 100% humidity. 4  $\mu\text{l}$   
21

22 605 complex sample was applied to the grids and the blotting was performed with a blot force of 0 for  
23

24 606 4 s prior to plunge freezing into liquid ethane. For WT-fl-Spike/CVD293 complex, two datasets  
25

26 607 comprising of 2,058 and 3,636 120-frame super-resolution movies each were collected while for  
27

28  
29 608 WT-fl-Spike/CVD432 complex, three datasets comprising of 4,915, 3,196, and 2,574 120-frame  
30

31 609 super-resolution movies each were collected. For both complexes movies were acquired in super-  
32

33 610 resolution mode on a Titan Krios (ThermoFisher) equipped with a K3 camera and a Bioquantum  
34

35 611 energy filter (Gatan) set to a slit width of 20 eV. Collection was performed with a 3x3 image shift  
36

37  
38 612 at a calibrated magnification of 105,000 x corresponding to a super resolution pixel size of 0.4265  
39

40 613  $\text{\AA}/\text{pix}$ . Collection dose rate was 8  $\text{e}^-/\text{physical pixel}/\text{second}$  for a total dose of 68  $\text{e}^-/\text{\AA}^2$ . Defocus  
41

42 614 range was -0.8 to -1.8  $\mu\text{m}$ . Movies were subsequently corrected for drift using MotionCor2 (Zheng  
43

44 615 et al., 2017) and were Fourier-cropped by a factor of 2 to a final pixel size of 0.834  $\text{\AA}/\text{pixel}$ . Each  
45

46 616 collection was performed with semi-automated scripts in SerialEM (Mastronarde, 2003, 2005).  
47

48  
49 617

50  
51 618 **Data Processing -**  
52

53 619

54  
55 620 **WT-fl-Spike/CVD293 complex 1-RBD-up state** (Figure S2): Initial processing was done in  
56

57  
58 621 cryoSPARC (v2.15.0) (Punjani et al., 2017, 2020). The two datasets with 3636 and 2058 dose-  
59

60 622 weighted motion corrected micrographs (Zheng et al., 2017) were imported and Patch CTF(M)  
61

62  
63  
64  
65

1  
2  
3  
4 623 was performed. Micrographs were curated based on CTF-fit resolution ( $<4 \text{ \AA}$ ), ice-thickness, and  
5  
6 624 presence of carbon. After manual curation, 3144 and 1575 micrographs were selected for further  
7  
8 625 processing. Blob-picker was used to pick 1,673,305 and 831,773 particles and extraction was  
9  
10 626 done with a box size of 580 px downsized to 480 px for each dataset. 2D-classification was done  
11  
12  
13 627 into 150 classes and good classes were selected with a total of 401,671 particles combined from  
14  
15 628 both datasets. Multiple rounds of heterogeneous, homogenous, and non-uniform refinements in  
16  
17 629 cryoSPARC and focused classification in cisTEM (Grant et al., 2018) resulted in a  $3.77 \text{ \AA}$  3D-  
18  
19 630 reconstruction of WT-fl-Spike/CVD293 with 61,033 particles. Particle subtraction/local refinement  
20  
21  
22 631 was performed on this final stack of particles focusing on the CVD293/RBD to obtain a  $3.50 \text{ \AA}$  3D  
23  
24 632 reconstruction of WT-Spike-RBD (residues 331-541)/CVD293 (residues 18-614).

25  
26 633  
27  
28  
29 634 **WT-fl-Spike/CVD432 complex 1-RBD-up state** (Figure S3): Initial processing was done in  
30  
31 635 cryoSPARC (v2.15.0). The three datasets with 4915, 3916 and 2574 dose-weighted motion  
32  
33 636 corrected micrographs were imported and Patch CTF(M) was performed. Micrographs were  
34  
35 637 curated based on CTF-fit resolution ( $<4 \text{ \AA}$ ), ice-thickness, and presence of carbon. After manual  
36  
37 638 curation, 3864, 2238 and 2148 micrographs were selected for further processing. Blob-picker was  
38  
39  
40 639 used to pick 1,259,441 particles from Dataset 1 while template-based particle picker ( $260 \text{ \AA}$   
41  
42 640 diameter) was used to pick 782,620 and 752,648 particles for Dataset 2 and Dataset 3,  
43  
44 641 respectively. Extraction was done with a box size of 512 px for Dataset 1 which was re-extracted  
45  
46 642 with box size of 600 px after a round of ab-initio refinement and finally downsampled to 400 px.  
47  
48  
49 643 For Datasets 2 and 3, extraction was done at box size 600 px and then downsampled to 400 px.  
50  
51 644 2D-classification was done with 150 classes for each dataset and good classes of WT-fl-  
52  
53 645 Spike/CVD432 in 1-RBD-up state were selected with a total of 601,624 particles combined from  
54  
55 646 the three datasets. Multiple rounds of heterogeneous, non-uniform refinements and homogenous  
56  
57 647 refinements in cryoSPARC and focused classification in cisTEM resulted in a  $3.5 \text{ \AA}$  3D-  
58  
59 648 reconstruction of WT-fl-Spike/CVD432 1-RBD-up state with 97,082 particles. Particle  
60  
61  
62  
63  
64  
65

1  
2  
3  
4 649 subtraction/local refinement was performed on this final stack of particles focusing on the  
5  
6 650 CVD432/RBD to obtain a 3.36 Å 3D reconstruction of WT-Spike-RBD (residues 331-  
7  
8 651 541)/CVD432 (residues 18-614).

10 652  
11  
12  
13 653 **WT-fl-Spike/CVD432 complex 2-RBD-up state** (Figure S4): We processed the WT-fl-  
14  
15 654 Spike/CVD432 complex 2-RBD-up state independent of the 1-RBD-up state. Initial processing  
16  
17 655 was done in cryoSPARC (v2.15.0). The three datasets with 4915, 3916 and 2574 dose-weighted  
18  
19 656 motion corrected micrographs were imported and Patch CTF(M) was performed. Micrographs  
20  
21 657 were curated based on CTF-fit resolution (<4 Å), ice-thickness, and presence of carbon. After  
22  
23 658 manual curation, 3833, 2253 and 2175 micrographs were selected for further processing. We first  
24  
25 659 used blob-picker on Dataset 1 to pick 1,597,143 and after 2D classification, 19 good classes were  
26  
27 660 selected. The 19 classes from Data set 1 were used for template-based particle picker (220 Å  
28  
29 661 diameter) to pick 1,499,401 and 1,019,564 and 1,328,287 particles for Dataset 1, Dataset 2 and  
30  
31 662 Dataset 3, respectively. Extraction was done at box size 600 px for all datasets. 2D-classification  
32  
33 663 was done into 150 classes for each dataset and good looking classes with WT-fl-Spike/CVD432  
34  
35 664 in 2-RBD-up state were selected with a total of 113,836 particles combined from the three  
36  
37 665 datasets. Multiple rounds of heterogeneous, non-uniform refinements and homogenous  
38  
39 666 refinements in cryoSPARC and focused classification in cisTEM resulted in a 2.97 Å 3D-  
40  
41 667 reconstruction of WT-fl-Spike/CVD432 2-up state with 97,374 particles. Each WT-Spike-  
42  
43 668 RBD/CVD432 interface in the 2-RBD-up state was at an overall low resolution and particle  
44  
45 669 subtraction/local refinement was not performed.

50  
51 670  
52  
53 671

54  
55 672 **Model Building and Refinement -**

56  
57 673  
58  
59 674 ***Low resolution rigid body fitting***

60  
61  
62  
63  
64  
65

1  
2  
3  
4  
5  
6  
7  
8  
9  
10  
11  
12  
13  
14  
15  
16  
17  
18  
19  
20  
21  
22  
23  
24  
25  
26  
27  
28  
29  
30  
31  
32  
33  
34  
35  
36  
37  
38  
39  
40  
41  
42  
43  
44  
45  
46  
47  
48  
49  
50  
51  
52  
53  
54  
55  
56  
57  
58  
59  
60  
61  
62  
63  
64  
65

675

676 1-RBD-up state WT-fl-Spike/WT-ACE2 model with PDB ID - 7DX5, was used as the initial model  
677 for rigid body fitting into cryo-EM density map of 1-RBD-up state of WT-fl-Spike/CVD293 or 1-  
678 RBD-up state of WT-fl-Spike/CVD432 in CHIMERA (Pettersen et al., 2004). For 2-RBD-up state  
679 of WT-fl-Spike/CVD432, we generated a model by rigid body fitting PDB ID - 7DX5 into the density  
680 map and simultaneously rigid body fitting WT-Spike-RBD/ACE2 (18-614) complex with PDB ID -  
681 6M0J into the second RBD-up region of the map in CHIMERA. The final model was fit using  
682 FastRelax in torsion space in Rosetta into the WT-fl-Spike/WT-ACE2 2-RBD-up state cryo-EM  
683 map. Rosetta into the Overall, the fits agree with previously reported 1-RBD-up states for WT-fl-  
684 Spike/ACE2 (18-614) complexes.

685

#### 686 **High resolution “final consensus” model building**

687

688 High resolution map of WT-Spike-RBD/CVD293 (18-614) with mutations K31F, H34I, E35Q or  
689 WT-Spike-RBD/CVD432 (18-614) with mutations K31F, N33D, H34S, E35Q were generated from  
690 WT-fl-Spike/CVD293 map or WT-fl-Spike/CVD432 map, respectively, in cryoSPARC (v2.15.0) by  
691 Particle subtraction/Local refinement. PDB ID: 6M0J was used for initial rigid body fit into the WT-  
692 Spike-RBD/CVD293 (18-614) map. This model was then refined against the respective maps in  
693 Phenix Real Space Refine (Liebschner et al., 2019) with the corrected sequence input for CVD293  
694 or CVD432. This was followed by a FastRelax in torsion space with Rosetta (2020.08 release)  
695 (Wang et al., 2016). Model for each complex was manually examined and corrected using COOT  
696 0.9 (Emsley et al., 2010) and ISOLDE 1.0 (Croll, 2018). The B-factors were assigned using a  
697 Rosetta B-factor fitting mover. Local resolution was determined by running the ResMap program  
698 (Kucukelbir et al., 2014). Directional FSC curves were determined by submitting the associated  
699 files to the 3DFSC server (Tan et al., 2017). Q-scores were calculated using the Q-score plugin  
700 for USCF Chimera (Pintilie et al., 2020).



1  
2  
3  
4  
5  
6  
7  
8  
9  
10  
11  
12  
13  
14  
15  
16  
17  
18  
19  
20  
21  
22  
23  
24  
25  
26  
27  
28  
29  
30  
31  
32  
33  
34  
35  
36  
37  
38  
39  
40  
41  
42  
43  
44  
45  
46  
47  
48  
49  
50  
51  
52  
53  
54  
55  
56  
57  
58  
59  
60  
61  
62  
63  
64  
65

701

## 702 **Multi-model Pipeline**

703

704 The Cryo-EM consensus model of WT-Spike-RBD/CVD293 (18-614) or WT-Spike-RBD/CVD432

705 (18-614) was used as the starting model for the pipeline. We applied the Rosetta Iterative Rebuild

706 protocol on 10-amino acid overlapping stretches of the interface helix for each consensus model.

707 The parameters used were defined in an XML file (Parameters.xml) found in SI Appendix:

708 Supplemental computational methods: Commands and input files section. For each 10-amino

709 acid stretch of the interface helix we generated 2000 independent models totaling 8000 models

710 for the entire interface helix from ACE2 residue 21 to residue 52. Total of 200 models were then

711 selected based on the total Rosetta energy score followed by the top 20 that best fit to the map

712 destiny. A total of 80 top selected models for each complex were then used for further analyses.

713 We calculated the local average per residue average side-chain RMSD in CHIMERA and average

714 interface energy (in REU) for the residues of the interface helix.

715

## 716 **Energy calculations**

717

718 Total and individual pairwise interface energies were calculated for all design models and cryo-

719 EM atomic models using the Rosetta interface energy application. Per-residue energies were

720 calculated using the Rosetta per-residue energy application, and total energies were calculated

721 using the Rosetta scoring application in Rosetta

722 (2021.48.post.dev+8.master.77491fa20be77491fa20be83588cfc37ab422ba5b95eca128ebgit@

723 github.com:RosettaCommons/main.git 2021-12-02T08:56:13) (Alford et al., 2017; Leman et al.,

724 2020) . For the cryo-EM atomic models of CVD293 and CVD432, all scores were averaged and

725 standard deviations were calculated. The command lines and code are available in the *SI*

726 *Appendix: Supplemental computational methods: Commands and input files section.*

1  
2  
3  
4 727  
5  
6 728 **Design models of the ACE2 domain of CVD432**

7  
8 729  
9  
10 730 Design models of the ACE2 domain of CVD432 were generated using the RosettaScripts  
11  
12 731 framework (Glasgow et al., 2020). Beginning with the atomic models of CVD293 solved by cryo-  
13  
14 732 EM using the multi-model pipeline, we mutated N33 and I34 to aspartic acid and serine,  
15  
16 733 respectively, in each of the 80 WT-Spike-RBD/CVD293 cryo-EM based models and minimized  
17  
18 734 the complexes. Total energies and interface energies were calculated as described in “Energy  
19  
20 735 calculations.” The average interface energies and standard deviation is shown as CVD293 cryo-  
21  
22 736 EM based models in Figure 3e. The code is available in the *SI Appendix: Supplemental*  
23  
24 737 *computational methods: Commands and input files section*.

25  
26 738  
27  
28 739 **Determination of binding affinity using biolayer interferometry (BLI)**

29  
30 740  
31  
32 741 Affinity measurements were carried out at room temperature using an Octet RED384 system. In  
33  
34 742 our BLI experiments, ACE2 Fc-fusions are tethered to either Streptavidin biosensors (WT-ACE2,  
35  
36 743 CVD293) (Sartorius®, Item no.: 18-5019) or ProtA biosensors (Sartorius®, Item no.: 18-5010)  
37  
38 744 and WT, Delta-, Omicron-SARS-CoV-2 spike RBD are present as the analyte in solution in a 384-  
39  
40 745 well microplate. The biosensors were washed in phosphate buffered saline (1X PBS) with 0.05%  
41  
42 746 Tween-20 at pH 7.4 and 0.2% bovine serum albumin (BSA) (1X PBSTB) for 200 seconds.  
43  
44 747 Antigens WT-ACE2, CVD293 were diluted to 10 nM in 1X PBSTB containing 10 µM biotin (1X  
45  
46 748 PBSTBB) as blocking agent while antigen CVD432 was diluted 10nM in 1X PBSTB. The antigens  
47  
48 749 were then loaded to the respective biosensors for 300 seconds. Following loading, a baseline was  
49  
50 750 established by washing the WT-ACE2 or CVD293 bound Streptavidin biosensors in 1X PBSTBB  
51  
52 751 and CVD432 bound ProtA biosensors in 1X PBSTB for 200 seconds. WT, Delta-, Omicron-SARS-  
53  
54 752 CoV-2 spike RBD were then allowed to associate with the antigen at concentrations ranging from  
55  
56  
57  
58  
59  
60  
61  
62  
63  
64  
65

1  
2  
3  
4 753 0 to 25 nM of Spike for about 600 seconds and then returned to the respective washing well to  
5  
6 754 follow dissociation for about 900 seconds. Raw data were fit in Octet Data Analysis HT software  
7  
8 755 version 10.0 using curve-fitting kinetic analysis with global fitting and assuming 1:1 non-  
9  
10 756 cooperative binding kinetics. All fits to BLI data had  $R^2$  (goodness of fit) > 0.90.  
11  
12

13 757

## 14 15 16 758 **Pseudovirus Production**

17  
18  
19 759 SARS-CoV-2 pseudoviruses bearing spike proteins of variants of interest were generated as  
20  
21 760 previously described (Hoffmann et al., 2020; Laurie et al., 2021, 2022) using a recombinant  
22  
23 761 vesicular stomatitis virus (VSV) expressing green fluorescent protein (GFP) in place of the VSV  
24  
25 762 glycoprotein (rVSV  $\Delta$  G-GFP). B.1 (WT, 1 spike mutation (D614G)), B.1.617.2/delta (9-10 spike  
26  
27 763 mutations), and B.1.1.529/ omicron (37 spike mutations) were cloned in a cytomegalovirus  
28  
29 764 enhancer-driven expression vector and used to produce SARS-CoV-2 spike pseudoviruses. The  
30  
31 765 mutations for each variant are listed as follows - B.1/WT (D614G), B.1.617.2/Delta (T19R, T95I,  
32  
33 766 G142D,  $\Delta$ 157-158, L452R, T478K, P681R, D614G, D950N), B.1.1.529/Omicron (A67V,  $\Delta$ H69,  
34  
35 767  $\Delta$ V70, T95I,  $\Delta$ G142,  $\Delta$ V143,  $\Delta$ Y144, Y145D,  $\Delta$ N211, L212I, G339D, S371L, S373P, S375F,  
36  
37 768 K417N, N440K, G446S, S477N, T478K, E484A, Q493R, G496S, Q498R, N501Y, Y505H, T547K,  
38  
39 769 D614G, H655Y, N679K, P681H, N764K, D796Y, N856K, Q954H, N969K, L981F). Pseudoviruses  
40  
41 770 were titered on Huh7.5.1 cells overexpressing ACE2 and TMPRSS2 (gift of Andreas Puschnik)  
42  
43 771 using GFP expression to measure the concentration of focus forming units (ffu).  
44  
45  
46  
47

## 48 49 772 **Pseudovirus Neutralization Assay**

50  
51 773  
52  
53 774 Pseudovirus Neutralization Assay was performed as described previously (Laurie et al., 2021,  
54  
55 775 2022) Huh7.5.1-ACE2-TMPRSS2 cells were seeded in 96-well plates at a density of 7000-8000  
56  
57 776 cells/well 1 day prior to pseudovirus infection. ACE2 receptor traps were serially diluted into  
58  
59 777 complete culture media (Dulbecco's Modified Eagle's Medium with 10% fetal bovine serum,  
60  
61  
62  
63  
64  
65

1  
2  
3  
4  
5  
6  
7  
8  
9  
10  
11  
12  
13  
14  
15  
16  
17  
18  
19  
20  
21  
22  
23  
24  
25  
26  
27  
28  
29  
30  
31  
32  
33  
34  
35  
36  
37  
38  
39  
40  
41  
42  
43  
44  
45  
46  
47  
48  
49  
50  
51  
52  
53  
54  
55  
56  
57  
58  
59  
60  
61  
62  
63  
64  
65

778 10mM HEPES, 1X Pen-Strep-Glutamine). Each pseudovirus was diluted to 125 ffu/ $\mu$ L and 30  $\mu$ L  
779 of each pseudovirus was mixed with  $\sim$ 30  $\mu$ L of ACE2 receptor traps or media only. Media only  
780 with no pseudovirus served as an additional control. These were incubated at 37°C for 1 hour  
781 before adding 50  $\mu$ L of virus:binder incubated mix directly to previously plated cells. Cells  
782 inoculated with ACE2 receptor traps/pseudovirus mixtures were incubated at 37°C and 5% CO<sub>2</sub>  
783 for 24 hours. The cells were then lifted and resuspended using 20  $\mu$ L of 10X TrypLE Select (Gibco)  
784 and GFP signal of infected cells recorded using Beckman CytoFlex Cytometer B4R3V4.  
785 Data were analyzed with FlowJo™ to determine percent GFP-positive pseudovirus transduced  
786 cells. GFP-signals from wells with no ACE2 receptor traps (media only with pseudovirus) were  
787 used to normalize the data and determine percent neutralization. A 7-8 point dose-response curve  
788 was generated in GraphPad Prism and IC50s reported in  $\mu$ g/mL. The reported IC50s are based  
789 on two technical and biological replicates for each pseudovirus/ACE2 receptor trap pair.

790

1  
2  
3  
4  
5  
6  
7  
8  
9  
10  
11  
12  
13  
14  
15  
16  
17  
18  
19  
20  
21  
22  
23  
24  
25  
26  
27  
28  
29  
30  
31  
32  
33  
34  
35  
36  
37  
38  
39  
40  
41  
42  
43  
44  
45  
46  
47  
48  
49  
50  
51  
52  
53  
54  
55  
56  
57  
58  
59  
60  
61  
62  
63  
64  
65

## 791 Bibliography

- 792 Alford, R.F., Leaver-Fay, A., Jeliazkov, J.R., O'Meara, M.J., DiMaio, F.P., Park, H., Shapovalov,  
793 M.V., Renfrew, P.D., Mulligan, V.K., Kappel, K., et al. (2017). The Rosetta All-Atom Energy  
794 Function for Macromolecular Modeling and Design. *J. Chem. Theory Comput.* *13*, 3031–3048.  
795 <https://doi.org/10.1021/acs.jctc.7b00125>.
- 796 Barnes, C.O., West, A.P., Huey-Tubman, K.E., Hoffmann, M.A.G., Sharaf, N.G., Hoffman, P.R.,  
797 Koranda, N., Gristick, H.B., Gaebler, C., Muecksch, F., et al. (2020a). Structures of Human  
798 Antibodies Bound to SARS-CoV-2 Spike Reveal Common Epitopes and Recurrent Features of  
799 Antibodies. *Cell* *182*, 828-842.e16. <https://doi.org/10.1016/j.cell.2020.06.025>.
- 800 Barnes, C.O., Jette, C.A., Abernathy, M.E., Dam, K.-M.A., Esswein, S.R., Gristick, H.B.,  
801 Malyutin, A.G., Sharaf, N.G., Huey-Tubman, K.E., Lee, Y.E., et al. (2020b). SARS-CoV-2  
802 neutralizing antibody structures inform therapeutic strategies. *Nature* *588*, 682–687.  
803 <https://doi.org/10.1038/s41586-020-2852-1>.
- 804 Barton, M.I., MacGowan, S.A., Kutuzov, M.A., Dushek, O., Barton, G.J., and van der Merwe,  
805 P.A. (2021). Effects of common mutations in the SARS-CoV-2 Spike RBD and its ligand, the  
806 human ACE2 receptor on binding affinity and kinetics. *ELife* *10*.  
807 <https://doi.org/10.7554/eLife.70658>.
- 808 Baum, A., Fulton, B.O., Wloga, E., Copin, R., Pascal, K.E., Russo, V., Giordano, S., Lanza, K.,  
809 Negron, N., Ni, M., et al. (2020). Antibody cocktail to SARS-CoV-2 spike protein prevents rapid  
810 mutational escape seen with individual antibodies. *Science* *369*, 1014–1018.  
811 <https://doi.org/10.1126/science.abd0831>.
- 812 Cameroni, E., Bowen, J.E., Rosen, L.E., Saliba, C., Zepeda, S.K., Culp, K., Pinto, D.,  
813 VanBlargan, L.A., De Marco, A., di Iulio, J., et al. (2022). Broadly neutralizing antibodies  
814 overcome SARS-CoV-2 Omicron antigenic shift. *Nature* *602*, 664–670.

1  
2  
3  
4 815 <https://doi.org/10.1038/s41586-021-04386-2>.  
5  
6  
7 816 Cao, Y., Wang, J., Jian, F., Xiao, T., Song, W., Yisimayi, A., Huang, W., Li, Q., Wang, P., An,  
8  
9 817 R., et al. (2022). Omicron escapes the majority of existing SARS-CoV-2 neutralizing antibodies.  
10  
11 818 *Nature* 602, 657–663. <https://doi.org/10.1038/s41586-021-04385-3>.  
12  
13  
14 819 Cele, S., Jackson, L., Khoury, D.S., Khan, K., Moyo-Gwete, T., Tegally, H., San, J.E., Cromer,  
15  
16 820 D., Scheepers, C., Amoako, D., et al. (2021). SARS-CoV-2 Omicron has extensive but  
17  
18 821 incomplete escape of Pfizer BNT162b2 elicited neutralization and requires ACE2 for infection.  
19  
20 822 *MedRxiv* <https://doi.org/10.1101/2021.12.08.21267417>.  
21  
22  
23 823 Chan, K.K., Dorosky, D., Sharma, P., Abbasi, S.A., Dye, J.M., Kranz, D.M., Herbert, A.S., and  
24  
25 824 Procko, E. (2020). Engineering human ACE2 to optimize binding to the spike protein of SARS  
26  
27 825 coronavirus 2. *Science* 369, 1261–1265. <https://doi.org/10.1126/science.abc0870>.  
28  
29  
30 826 Chowdhury, R., Boorla, V.S., Maranas, C.D. (2020). Computational biophysical characterization  
31  
32 827 of the SARS-CoV-2 spike protein binding with the ACE2 receptor and implications for infectivity.  
33  
34 828 *Comput Struct Biotechnol J.* 18, 2573-2582.  
35  
36  
37 829 Cohen, M.S., Nirula, A., Mulligan, M.J., Novak, R.M., Marovich, M., Yen, C., Stemer, A., Mayer,  
38  
39 830 S.M., Wohl, D., Brengle, B., et al. (2021). Effect of Bamlanivimab vs Placebo on Incidence of  
40  
41 831 COVID-19 Among Residents and Staff of Skilled Nursing and Assisted Living Facilities: A  
42  
43 832 Randomized Clinical Trial. *JAMA* 326, 46–55. <https://doi.org/10.1001/jama.2021.8828>.  
44  
45  
46 833 Croll, T.I. (2018). ISOLDE: a physically realistic environment for model building into low-  
47  
48 834 resolution electron-density maps. *Acta Crystallogr. D Struct. Biol.* 74, 519–530.  
49  
50 835 <https://doi.org/10.1107/S2059798318002425>.  
51  
52  
53 836 DiMaio, F., Song, Y., Li, X., Brunner, M.J., Xu, C., Conticello, V., Egelman, E., Marlovits, T.,  
54  
55 837 Cheng, Y., and Baker, D. (2015). Atomic-accuracy models from 4.5-Å cryo-electron microscopy  
56  
57 838 data with density-guided iterative local refinement. *Nat. Methods* 12, 361–365.  
58  
59  
60  
61  
62  
63  
64  
65

- 1  
2  
3  
4 839 <https://doi.org/10.1038/nmeth.3286>.
- 5  
6  
7 840 Dong, J., Zost, S.J., Greaney, A.J., Starr, T.N., Dingens, A.S., Chen, E.C., Chen, R.E., Case,  
8  
9 841 J.B., Sutton, R.E., Gilchuk, P., et al. (2021). Genetic and structural basis for SARS-CoV-2  
10  
11 842 variant neutralization by a two-antibody cocktail. *Nat. Microbiol.* 6, 1233–1244.  
12  
13  
14 843 <https://doi.org/10.1038/s41564-021-00972-2>.
- 15  
16 844 Emsley, P., Lohkamp, B., Scott, W.G., and Cowtan, K. (2010). Features and development of  
17  
18 845 Coot. *Acta Crystallogr. D Biol. Crystallogr.* 66, 486–501.  
19  
20  
21 846 <https://doi.org/10.1107/S0907444910007493>.
- 22  
23 847 Glasgow, A., Glasgow, J., Limonta, D., Solomon, P., Lui, I., Zhang, Y., Nix, M.A., Rettko, N.J.,  
24  
25 848 Zha, S., Yamin, R., et al. (2020). Engineered ACE2 receptor traps potently neutralize SARS-  
26  
27 849 CoV-2. *Proc Natl Acad Sci USA* 117, 28046–28055. <https://doi.org/10.1073/pnas.2016093117>.
- 28  
29  
30  
31 850 Gottlieb, R.L., Nirula, A., Chen, P., Boscia, J., Heller, B., Morris, J., Huhn, G., Cardona, J.,  
32  
33 851 Mocherla, B., Stosor, V., et al. (2021). Effect of Bamlanivimab as Monotherapy or in  
34  
35 852 Combination With Etesevimab on Viral Load in Patients With Mild to Moderate COVID-19: A  
36  
37 853 Randomized Clinical Trial. *JAMA* 325, 632–644. <https://doi.org/10.1001/jama.2021.0202>.
- 38  
39  
40 854 Grant, T., Rohou, A., and Grigorieff, N. (2018). cisTEM, user-friendly software for single-particle  
41  
42 855 image processing. *ELife* 7, e35383. <https://doi.org/10.7554/eLife.35383>.
- 43  
44  
45 856 Hansen, J., Baum, A., Pascal, K.E., Russo, V., Giordano, S., Wloga, E., Fulton, B.O., Yan, Y.,  
46  
47 857 Koon, K., Patel, K., et al. (2020). Studies in humanized mice and convalescent humans yield a  
48  
49 858 SARS-CoV-2 antibody cocktail. *Science* 369, 1010–1014.  
50  
51  
52 859 <https://doi.org/10.1126/science.abd0827>.
- 53  
54  
55 860 Herzik, M.A., Fraser, J.S., and Lander, G.C. (2019). A Multi-model Approach to Assessing Local  
56  
57 861 and Global Cryo-EM Map Quality. *Structure* 27, 344-358.e3.  
58  
59 862 <https://doi.org/10.1016/j.str.2018.10.003>.
- 60  
61  
62  
63  
64  
65

- 1  
2  
3  
4 863 Higuchi, Y., Suzuki, T., Arimori, T., Ikemura, N., Mihara, E., Kirita, Y., Ohgitani, E., Mazda, O.,  
5  
6 864 Motooka, D., Nakamura, S., et al. (2021). Engineered ACE2 receptor therapy overcomes  
7  
8 865 mutational escape of SARS-CoV-2. *Nat. Commun.* *12*, 3802. [https://doi.org/10.1038/s41467-](https://doi.org/10.1038/s41467-021-24013-y)  
9  
10 866 021-24013-y.  
11  
12  
13  
14 867 Hoffmann, M., Kleine-Weber, H., and Pöhlmann, S. (2020). A Multibasic Cleavage Site in the  
15  
16 868 Spike Protein of SARS-CoV-2 Is Essential for Infection of Human Lung Cells. *Mol. Cell* *78*, 779-  
17  
18 869 784.e5. <https://doi.org/10.1016/j.molcel.2020.04.022>.  
19  
20  
21 870 Ikemura, N., Taminishi, S., Inaba, T., Arimori, T., Motooka, D., Katoh, K., Kirita, Y., Higuchi, Y.,  
22  
23 871 Li, S., Itoh, Y., et al. (2021). Engineered ACE2 counteracts vaccine-evading SARS-CoV-2  
24  
25 872 Omicron variant. *BioRxiv* <https://doi.org/10.1101/2021.12.22.473804>.  
26  
27  
28 873 Jones, B.E., Brown-Augsburger, P.L., Corbett, K.S., Westendorf, K., Davies, J., Cujec, T.P.,  
29  
30 874 Wiethoff, C.M., Blackbourne, J.L., Heinz, B.A., Foster, D., et al. (2021). The neutralizing  
31  
32 875 antibody, LY-CoV555, protects against SARS-CoV-2 infection in nonhuman primates. *Sci.*  
33  
34 876 *Transl. Med.* *13*. <https://doi.org/10.1126/scitranslmed.abf1906>.  
35  
36  
37 877 Koerber, J.T., Thomsen, N.D., Hannigan, B.T., Degrado, W.F., and Wells, J.A. (2013). Nature-  
38  
39 878 inspired design of motif-specific antibody scaffolds. *Nat. Biotechnol.* *31*, 916–921.  
40  
41 879 <https://doi.org/10.1038/nbt.2672>.  
42  
43  
44 880 Kucukelbir, A., Sigworth, F.J., and Tagare, H.D. (2014). Quantifying the local resolution of cryo-  
45  
46 881 EM density maps. *Nat. Methods* *11*, 63–65. <https://doi.org/10.1038/nmeth.2727>.  
47  
48  
49 882 Laffeber, C., de Koning, K., Kanaar, R., and Lebbink, J.H.G. (2021). Experimental Evidence for  
50  
51 883 Enhanced Receptor Binding by Rapidly Spreading SARS-CoV-2 Variants. *J. Mol. Biol.* *433*,  
52  
53 884 167058. <https://doi.org/10.1016/j.jmb.2021.167058>.  
54  
55  
56 885 Laurie, M.T., Liu, J., Sunshine, S., Peng, J., Black, D., Mitchell, A.M., Mann, S.A., Pilarowski,  
57  
58 886 G., Zorn, K.C., Rubio, L., et al. (2021). SARS-CoV-2 variant exposures elicit antibody responses  
59  
60  
61  
62  
63  
64  
65



1  
2  
3  
4 887 with differential cross-neutralization of established and emerging strains including Delta and  
5  
6 888 Omicron. MedRxiv <https://doi.org/10.1101/2021.09.08.21263095>.  
7  
8  
9 889 Laurie, M.T., Liu, J., Sunshine, S., Peng, J., Black, D., Mitchell, A.M., Mann, S.A., Pilarowski,  
10  
11 890 G., Zorn, K.C., Rubio, L., et al. (2022). SARS-CoV-2 Variant Exposures Elicit Antibody  
12  
13 891 Responses With Differential Cross-Neutralization of Established and Emerging Strains Including  
14  
15 892 Delta and Omicron. *J. Infect. Dis.* 225, 1909–1914. <https://doi.org/10.1093/infdis/jiab635>.  
16  
17  
18 893 Lei, C., Qian, K., Li, T., Zhang, S., Fu, W., Ding, M., and Hu, S. (2020). Neutralization of SARS-  
19  
20 894 CoV-2 spike pseudotyped virus by recombinant ACE2-Ig. *Nat. Commun.* 11, 2070.  
21  
22  
23 895 <https://doi.org/10.1038/s41467-020-16048-4>.  
24  
25  
26 896 Leman, J.K., Weitzner, B.D., Lewis, S.M., Adolf-Bryfogle, J., Alam, N., Alford, R.F., Aprahamian,  
27  
28 897 M., Baker, D., Barlow, K.A., Barth, P., et al. (2020). Macromolecular modeling and design in  
29  
30 898 Rosetta: recent methods and frameworks. *Nat. Methods* 17, 665–680.  
31  
32 899 <https://doi.org/10.1038/s41592-020-0848-2>.  
33  
34  
35 900 Liebschner, D., Afonine, P.V., Baker, M.L., Bunkóczi, G., Chen, V.B., Croll, T.I., Hintze, B.,  
36  
37 901 Hung, L.W., Jain, S., McCoy, A.J., et al. (2019). Macromolecular structure determination using  
38  
39 902 X-rays, neutrons and electrons: recent developments in Phenix. *Acta Crystallogr. D Struct. Biol.*  
40  
41 903 75, 861–877. <https://doi.org/10.1107/S2059798319011471>.  
42  
43  
44 904 Liu, H., Zhang, Q., Wei, P., Chen, Z., Aviszus, K., Yang, J., Downing, W., Jiang, C., Liang, B.,  
45  
46 905 Reynoso, L., et al. (2021). The basis of a more contagious 501Y.V1 variant of SARS-CoV-2.  
47  
48 906 *Cell Res.* 31, 720–722. <https://doi.org/10.1038/s41422-021-00496-8>.  
49  
50  
51 907 Liu, L., Wang, P., Nair, M.S., Yu, J., Rapp, M., Wang, Q., Luo, Y., Chan, J.F.-W., Sahi, V.,  
52  
53 908 Figueroa, A., et al. (2020). Potent neutralizing antibodies against multiple epitopes on SARS-  
54  
55 909 CoV-2 spike. *Nature* 584, 450–456. <https://doi.org/10.1038/s41586-020-2571-7>.  
56  
57  
58 910 Liu, L., Iketani, S., Guo, Y., Chan, J.F.-W., Wang, M., Liu, L., Luo, Y., Chu, H., Huang, Y., Nair,  
59  
60  
61  
62  
63  
64  
65

1  
2  
3  
4  
5  
6  
7  
8  
9  
10  
11  
12  
13  
14  
15  
16  
17  
18  
19  
20  
21  
22  
23  
24  
25  
26  
27  
28  
29  
30  
31  
32  
33  
34  
35  
36  
37  
38  
39  
40  
41  
42  
43  
44  
45  
46  
47  
48  
49  
50  
51  
52  
53  
54  
55  
56  
57  
58  
59  
60  
61  
62  
63  
64  
65

911 M.S., et al. (2022). Striking antibody evasion manifested by the Omicron variant of SARS-CoV-  
912 2. *Nature* 602, 676–681. <https://doi.org/10.1038/s41586-021-04388-0>.

913 Mannar, D., Saville, J.W., Zhu, X., Srivastava, S.S., Berezuk, A.M., Zhou, S., Tuttle, K.S., Kim,  
914 A., Li, W., Dimitrov, D.S., et al. (2021). Structural analysis of receptor binding domain mutations  
915 in SARS-CoV-2 variants of concern that modulate ACE2 and antibody binding. *Cell Rep.* 37,  
916 110156. <https://doi.org/10.1016/j.celrep.2021.110156>.

917 Mannar, D., Saville, J.W., Zhu, X., Srivastava, S.S., Berezuk, A.M., Tuttle, K.S., Marquez, A.C.,  
918 Sekirov, I., and Subramaniam, S. (2022). SARS-CoV-2 Omicron variant: Antibody evasion and  
919 cryo-EM structure of spike protein-ACE2 complex. *Science* 375, 760–764.  
920 <https://doi.org/10.1126/science.abn7760>.

921 Mastronarde, D.N. (2003). SerialEM: A program for automated tilt series acquisition on tecnai  
922 microscopes using prediction of specimen position. *Microsc. Microanal.* 9, 1182–1183.  
923 <https://doi.org/10.1017/S1431927603445911>.

924 Mastronarde, D.N. (2005). Automated electron microscope tomography using robust prediction  
925 of specimen movements. *J. Struct. Biol.* 152, 36–51. <https://doi.org/10.1016/j.jsb.2005.07.007>.

926 McCallum, M., Walls, A.C., Sprouse, K.R., Bowen, J.E., Rosen, L.E., Dang, H.V., De Marco, A.,  
927 Franko, N., Tilles, S.W., Logue, J., et al. (2021). Molecular basis of immune evasion by the  
928 Delta and Kappa SARS-CoV-2 variants. *Science* 374, 1621–1626.  
929 <https://doi.org/10.1126/science.abl8506>.

930 McCallum, M., Czudnochowski, N., Rosen, L.E., Zepeda, S.K., Bowen, J.E., Walls, A.C.,  
931 Hauser, K., Joshi, A., Stewart, C., Dillen, J.R., et al. (2022). Structural basis of SARS-CoV-2  
932 Omicron immune evasion and receptor engagement. *Science* 375, 864–868.  
933 <https://doi.org/10.1126/science.abn8652>.

934 Mlcochova, P., Kemp, S.A., Dhar, M.S., Papa, G., Meng, B., Ferreira, I.A.T.M., Datir, R., Collier,

- 1  
2  
3  
4 935 D.A., Albecka, A., Singh, S., et al. (2021). SARS-CoV-2 B.1.617.2 Delta variant replication and  
5  
6 936 immune evasion. *Nature* 599, 114–119. <https://doi.org/10.1038/s41586-021-03944-y>.  
7  
8  
9 937 Mou, Y., Zhou, X.X., Leung, K., Martinko, A.J., Yu, J.-Y., Chen, W., and Wells, J.A. (2018).  
10  
11 938 Engineering improved antiphosphotyrosine antibodies based on an immunconvergent binding  
12  
13 939 motif. *J. Am. Chem. Soc.* 140, 16615–16624. <https://doi.org/10.1021/jacs.8b08402>.  
14  
15  
16 940 Park, Y.-J., De Marco, A., Starr, T.N., Liu, Z., Pinto, D., Walls, A.C., Zatta, F., Zepeda, S.K.,  
17  
18 941 Bowen, J.E., Sprouse, K.R., et al. (2022). Antibody-mediated broad sarbecovirus neutralization  
19  
20 942 through ACE2 molecular mimicry. *Science* 375, 449–454.  
21  
22  
23 943 <https://doi.org/10.1126/science.abm8143>.  
24  
25  
26 944 Pettersen, E.F., Goddard, T.D., Huang, C.C., Couch, G.S., Greenblatt, D.M., Meng, E.C., and  
27  
28 945 Ferrin, T.E. (2004). UCSF Chimera—a visualization system for exploratory research and  
29  
30 946 analysis. *J. Comput. Chem.* 25, 1605–1612. <https://doi.org/10.1002/jcc.20084>.  
31  
32  
33 947 Pintilie, G., Zhang, K., Su, Z., Li, S., Schmid, M.F., and Chiu, W. (2020). Measurement of atom  
34  
35 948 resolvability in cryo-EM maps with Q-scores. *Nat. Methods* 17, 328–334.  
36  
37 949 <https://doi.org/10.1038/s41592-020-0731-1>.  
38  
39  
40 950 Planas, D., Saunders, N., Maes, P., Guivel-Benhassine, F., Planchais, C., Buchrieser, J.,  
41  
42 951 Bolland, W.-H., Porrot, F., Staropoli, I., Lemoine, F., et al. (2022). Considerable escape of  
43  
44 952 SARS-CoV-2 Omicron to antibody neutralization. *Nature* 602, 671–675.  
45  
46 953 <https://doi.org/10.1038/s41586-021-04389-z>.  
47  
48  
49 954 Punjani, A., and Fleet, D.J. (2021). 3D variability analysis: Resolving continuous flexibility and  
50  
51 955 discrete heterogeneity from single particle cryo-EM. *J. Struct. Biol.* 213, 107702.  
52  
53 956 <https://doi.org/10.1016/j.jsb.2021.107702>.  
54  
55  
56 957 Punjani, A., Rubinstein, J.L., Fleet, D.J., and Brubaker, M.A. (2017). cryoSPARC: algorithms for  
57  
58 958 rapid unsupervised cryo-EM structure determination. *Nat. Methods* 14, 290–296.  
59  
60  
61  
62  
63  
64  
65

1  
2  
3  
4  
5  
6  
7  
8  
9  
10  
11  
12  
13  
14  
15  
16  
17  
18  
19  
20  
21  
22  
23  
24  
25  
26  
27  
28  
29  
30  
31  
32  
33  
34  
35  
36  
37  
38  
39  
40  
41  
42  
43  
44  
45  
46  
47  
48  
49  
50  
51  
52  
53  
54  
55  
56  
57  
58  
59  
60  
61  
62  
63  
64  
65

959 <https://doi.org/10.1038/nmeth.4169>.

960 Punjani, A., Zhang, H., and Fleet, D.J. (2020). Non-uniform refinement: adaptive regularization

961 improves single-particle cryo-EM reconstruction. *Nat. Methods* 17, 1214–1221.

962 <https://doi.org/10.1038/s41592-020-00990-8>.

963 Shi, R., Shan, C., Duan, X., Chen, Z., Liu, P., Song, J., Song, T., Bi, X., Han, C., Wu, L., et al.

964 (2020). A human neutralizing antibody targets the receptor-binding site of SARS-CoV-2. *Nature*

965 584, 120–124. <https://doi.org/10.1038/s41586-020-2381-y>.

966 Tan, Y.Z., Baldwin, P.R., Davis, J.H., Williamson, J.R., Potter, C.S., Carragher, B., and Lyumkis,

967 D. (2017). Addressing preferred specimen orientation in single-particle cryo-EM through tilting.

968 *Nat. Methods* 14, 793–796. <https://doi.org/10.1038/nmeth.4347>.

969 Tian, F., Tong, B., Sun, L., Shi, S., Zheng, B., Wang, Z., Dong, X., and Zheng, P. (2021). N501Y

970 mutation of spike protein in SARS-CoV-2 strengthens its binding to receptor ACE2. *ELife* 10.

971 <https://doi.org/10.7554/eLife.69091>.

972 Tortorici, M.A., Beltramello, M., Lempp, F.A., Pinto, D., Dang, H.V., Rosen, L.E., McCallum, M.,

973 Bowen, J., Minola, A., Jaconi, S., et al. (2020). Ultrapotent human antibodies protect against

974 SARS-CoV-2 challenge via multiple mechanisms. *Science* 370, 950–957.

975 <https://doi.org/10.1126/science.abe3354>.

976 VanBlargan, L.A., Errico, J.M., Halfmann, P., Zost, S.J., Crowe, J.E., Purcell, L.A., Kawaoka, Y.,

977 Corti, D., Fremont, D.H., and Diamond, M. (2021). An infectious SARS-CoV-2 B.1.1.529

978 Omicron virus escapes neutralization by several therapeutic monoclonal antibodies. *BioRxiv*

979 <https://doi.org/10.1101/2021.12.15.472828>.

980 Viana, R., Moyo, S., Amoako, D.G., Tegally, H., Scheepers, C., Althaus, C.L., Anyaneji, U.J.,

981 Bester, P.A., Boni, M.F., Chand, M., et al. (2022). Rapid epidemic expansion of the SARS-CoV-

982 2 Omicron variant in southern Africa. *Nature* 603, 679–686. <https://doi.org/10.1038/s41586-022->

- 1  
2  
3  
4 983 04411-y.  
5  
6  
7 984 Walls, A.C., Park, Y.-J., Tortorici, M.A., Wall, A., McGuire, A.T., and Veesler, D. (2020).  
8  
9 985 Structure, Function, and Antigenicity of the SARS-CoV-2 Spike Glycoprotein. *Cell* 181, 281-  
10  
11 986 292.e6. <https://doi.org/10.1016/j.cell.2020.02.058>.  
12  
13  
14 987 Wang, R.Y.-R., Song, Y., Barad, B.A., Cheng, Y., Fraser, J.S., and DiMaio, F. (2016).  
15  
16 988 Automated structure refinement of macromolecular assemblies from cryo-EM maps using  
17  
18 989 Rosetta. *ELife* 5. <https://doi.org/10.7554/eLife.17219>.  
19  
20  
21 990 Weidenbacher, P.A.-B., Waltari, E., de los Rios Kobara, I., Bell, B.N., Pak, J.E., and Kim, P.S.  
22  
23 991 (2022). Converting non-neutralizing SARS-CoV-2 antibodies targeting conserved epitopes into  
24  
25 992 broad-spectrum inhibitors through receptor blockade. *BioRxiv*  
26  
27 993 <https://doi.org/10.1101/2022.01.24.477625>.  
28  
29  
30  
31 994 Weinberg, Z.Y., Hilburger, C.E., Kim, M., Cao, L., Khalid, M., Elmes, S., Diwanji, D., Hernandez,  
32  
33 995 E., Lopez, J., Schaefer, K., et al. (2021). Sentinel cells enable genetic detection of SARS-CoV-2  
34  
35 996 Spike protein. *BioRxiv* <https://doi.org/10.1101/2021.04.20.440678>.  
36  
37  
38 997 Wilhelm, A., Widera, M., Grikscheit, K., Toptan, T., Schenk, B., Pallas, C., Metzler, M., Kohmer,  
39  
40 998 N., Hoehl, S., Helfritz, F.A., et al. (2021). Reduced Neutralization of SARS-CoV-2 Omicron  
41  
42 999 Variant by Vaccine Sera and monoclonal antibodies. *MedRxiv*  
43  
44 1000 <https://doi.org/10.1101/2021.12.07.21267432>.  
45  
46  
47 1001 Wirnsberger, G., Monteil, V., Eaton, B., Postnikova, E., Murphy, M., Braunsfeld, B., Crozier, I.,  
48  
49 1002 Kricek, F., Niederhöfer, J., Schwarzböck, A., et al. (2021). Clinical grade ACE2 as a universal  
50  
51 1003 agent to block SARS-CoV-2 variants. *BioRxiv* <https://doi.org/10.1101/2021.09.10.459744>.  
52  
53  
54 1004 Yan, R., Zhang, Y., Li, Y., Ye, F., Guo, Y., Xia, L., Zhong, X., Chi, X., and Zhou, Q. (2021).  
55  
56 1005 Structural basis for the different states of the spike protein of SARS-CoV-2 in complex with  
57  
58 1006 ACE2. *Cell Res.* 31, 717–719. <https://doi.org/10.1038/s41422-021-00490-0>.  
59  
60  
61  
62  
63  
64  
65

- 1  
2  
3  
4 1007 Zhang, L., Narayanan, K.K., Cooper, L., Chan, K.K., Devlin, C.A., Aguhob, A., Shirley, K., Rong,  
5  
6 1008 L., Rehman, J., Malik, A.B., et al. (2022). An engineered ACE2 decoy receptor can be  
7  
8 1009 administered by inhalation and potently targets the BA.1 and BA.2 omicron variants of SARS-  
10  
11 1010 CoV-2. *BioRxiv* <https://doi.org/10.1101/2022.03.28.486075>.  
12  
13  
14 1011 Zheng, S.Q., Palovcak, E., Armache, J.-P., Verba, K.A., Cheng, Y., and Agard, D.A. (2017).  
15  
16 1012 MotionCor2: anisotropic correction of beam-induced motion for improved cryo-electron  
17  
18 1013 microscopy. *Nat. Methods* *14*, 331–332. <https://doi.org/10.1038/nmeth.4193>.  
19  
20  
21 1014 Zhou, T., Tsybovsky, Y., Gorman, J., Rapp, M., Cerutti, G., Chuang, G.-Y., Katsamba, P.S.,  
22  
23 1015 Sampson, J.M., Schön, A., Bimela, J., et al. (2020a). Cryo-EM Structures of SARS-CoV-2 Spike  
24  
25 1016 without and with ACE2 Reveal a pH-Dependent Switch to Mediate Endosomal Positioning of  
26  
27 1017 Receptor-Binding Domains. *Cell Host Microbe* *28*, 867-879.e5.  
28  
29 1018 <https://doi.org/10.1016/j.chom.2020.11.004>.  
30  
31  
32 1019 Zhou, X.X., Bracken, C.J., Zhang, K., Zhou, J., Mou, Y., Wang, L., Cheng, Y., Leung, K.K., and  
33  
34 1020 Wells, J.A. (2020b). Targeting Phosphotyrosine in Native Proteins with Conditional, Bispecific  
35  
36 1021 Antibody Traps. *J. Am. Chem. Soc.* *142*, 17703–17713. <https://doi.org/10.1021/jacs.0c08458>.  
37  
38  
39 1022 Zhu, X., Mannar, D., Srivastava, S.S., Berezuk, A.M., Demers, J.-P., Saville, J.W., Leopold, K.,  
40  
41 1023 Li, W., Dimitrov, D.S., Tuttle, K.S., et al. (2021). Cryo-electron microscopy structures of the  
42  
43 1024 N501Y SARS-CoV-2 spike protein in complex with ACE2 and 2 potent neutralizing antibodies.  
44  
45 1025 *PLoS Biol.* *19*, e3001237. <https://doi.org/10.1371/journal.pbio.3001237>.  
46  
47  
48 1026 Zost, S.J., Gilchuk, P., Case, J.B., Binshtein, E., Chen, R.E., Nkolola, J.P., Schäfer, A., Reidy,  
49  
50 1027 J.X., Trivette, A., Nargi, R.S., et al. (2020). Potently neutralizing and protective human  
51  
52 1028 antibodies against SARS-CoV-2. *Nature* *584*, 443–449. <https://doi.org/10.1038/s41586-020->  
53  
54 1029 2548-6.  
55  
56  
57  
58  
59  
60  
61  
62  
63  
64  
65